Environmental Research 267 (2025) 120542

Contents lists available at ScienceDirect

Environmental Research

journal homepage: www.elsevier.com/locate/envres

Abatement of methylene blue and diazinon pesticide from synthetic solutions using magnetic biochar from pistachio shells modified with MOF-808

Sattam Fahad Almojil *, Abdulaziz Ibrahim Almohana

Department of Civil Engineering, College of Engineering, King Saud University, P.O. Box 800, Riyadh, 11421, Saudi Arabia

ARTICLE INFO

Keywords:
Metal-organic framework (MOF)
Aqueous solution
Pesticide
Magnetic composite
Kinetic analysis
Pistachio shell

ABSTRACT

This study develops a magnetic composite from pistachio shell biochar (PSBC/$CoFe_2O_4$) modified with MOF-808 for removing methylene blue (MB) dye and diazinon (DA) pesticide from water. The composite, with a surface area of 151.53 m^2/g and magnetic saturation of 19.653 emu/g, allowed easy separation from solutions. Key adsorption factors such as pH, temperature, contact time, adsorbent dosage, and initial pollutant concentration were optimized. Maximum removal efficiencies of 99.32% for MB and 99.14% for DA were achieved at adsorbent dosages of 1 g/L for MB and 1.5 g/L for DA, initial concentrations of 5 mg/L, temperatures of 55 °C, contact times of 60 min for MB and 80 min for DA, and pH levels of 9 for MB and 6 for DA. Thermodynamic analysis confirmed that the adsorption process is spontaneous and endothermic, with enthalpy values of 55.091 kJ/mol for MB and 42.028 kJ/mol for DA, while entropy values indicated increased randomness during adsorption. Kinetic studies revealed that adsorption involved both physical and chemical interactions, with intraparticle diffusion not being the rate-limiting step. The Freundlich isotherm model provided the best fit ($R^2 = 0.971$ for MB and 0.988 for DA), highlighting heterogeneous surface interactions. The composite showed higher adsorption capacities for MB (31.44 mg/g) than for DA (21.49 mg/g) and exhibited excellent regeneration potential, performing better in deionized water due to the inhibitory effects of salts in non-deionized water.

1. Introduction

Water, an essential resource for all life on Earth, is under increasing pressure due to rising global demand (Singh et al., 2024; Liu et al., 2008; Fan et al., 2024a). Rapid population growth and industrialization have led to the release of harmful wastewater from sources such as industries, households, hospitals, textiles, and agriculture. This pollution poses significant risks to public health and ecosystems, with long-term implications (Inamdar et al., 2023; Nguyen et al., 2024; Wang et al., 2024a; Huang et al., 2024a). Among these pollutants, the discharge of dyes into surface and groundwater has become a critical environmental issue. Approximately 50,000 tons of untreated organic dyes are released annually by industries such as textiles, pharmaceuticals, paper, plastics, and leather, threatening aquatic ecosystems (Badamasi et al., 2024; Ye et al., 2024). Research indicates that the benzene rings in many dyes contribute to their toxicity, mutagenicity, resistance to degradation, and carcinogenic potential in humans (Sharma et al., 2024). Methylene blue (MB), a widely used cationic dye in the textile and pharmaceutical sectors, is of particular concern, as its presence in water can lead to health issues such as cyanosis, tissue damage, jaundice, vomiting, and elevated heart rates in humans (Selvaraj et al., 2024).

Beyond organic dyes, the persistence of pesticides in wastewater presents a significant environmental challenge, often resulting in contamination of water and food sources (Adibzadeh et al., 2024). Diazinon (DA), an organophosphate pesticide, is extensively used in agricultural and non-agricultural sectors to boost crop and livestock productivity (Khaledian et al., 2021). The World Health Organization (WHO) sets the acceptable limit for diazinon in water at 20 μg/L, as exceeding this threshold can lead to adverse health effects such as nausea, vomiting, and neurological disorders (Salehzadeh et al., 2024). Consequently, there is an urgent need for effective methods to remove such pollutants from water sources, ensuring water quality, safeguarding ecosystems, and protecting public health.

Various techniques have been proposed for removing pollutants from

This article is part of a special issue entitled: WWEM-GEET-GC-2024 published in Environmental Research.

* Corresponding author.
E-mail address: salmojil@ksu.edu.sa (S.F. Almojil).

https://doi.org/10.1016/j.envres.2024.120542
Received 17 October 2024; Received in revised form 21 November 2024; Accepted 3 December 2024
Available online 18 December 2024

water, including filtration, ion exchange, degradation processes, phytoremediation, and adsorption (Wang et al., 2016). Among these, adsorption stands out as a cost-effective and eco-friendly method, valued for its simplicity, affordability, and minimal environmental impact (Wei et al., 2024). The success of adsorption relies heavily on the adsorbent's efficiency, underscoring the need to develop high-performance adsorbents to effectively eliminate pollutants and safeguard water resources for future generations (Su et al., 2024a; Ahmed and Ferdous, 2024).

Biochar (BC) has emerged as a promising adsorbent for effectively removing various organic and inorganic pollutants from industrial wastewater and aqueous solutions. It is produced through the thermal decomposition of diverse biomass sources, including fish bones (Bazarin et al., 2024), coconut straw (Duwiejuah et al., 2024), waste sludge (Wang et al., 2023), bamboo shoot shell (Hu et al., 2022), waste walnut shell (Zhang et al., 2024a), and biosolids (Damahe et al., 2024). The use of biochar derived from agricultural waste offers not only cost-efficiency but also notable properties such as high porosity, large active surface area, and abundant functional groups, making it a focal point for researchers (Jalayeri and Pepe, 2019). Among agricultural by-products, pistachio shells, generated at a global rate of approximately one million tons annually, are a rich resource containing unsaturated fatty acids, lignin, cellulose, hemicellulose, and dietary fibers. Despite their potential, these materials are underutilized in industrial applications and are often discarded through incineration. Transforming pistachio shells into biochar not only adds value to agricultural waste but also supports sustainable waste management practices (Saghir et al., 2022). However, BC's effectiveness as an adsorbent is limited when dealing with high contaminant concentrations in aqueous solutions due to its relatively low adsorption capacity (Saikia et al., 2017). To address this, various modification techniques have been proposed to enhance the adsorption performance of biochar, thereby broadening its applicability in water treatment (de Benedicto et al., 2024).

Metal-organic frameworks (MOFs) are porous, crystalline materials composed of metal ions and organic linkers, gaining significant attention for applications in photocatalysis, adsorption, and energy storage (Yu et al., 2022). Their unique attributes, including a high active surface area, well-defined structures, tunable chemical properties, and exceptional porosity, make MOFs highly effective as adsorbents (Sağlam et al., 2023). Among the various MOFs, zirconium-based MOF-808 stands out due to its remarkable features such as biocompatibility, extensive water stability, high porosity, large pore volume, superior surface area, and robust chemical and thermal stability (Kazemi et al., 2024; Pan et al., 2024; Wang et al., 2024b). MOF-808 is synthesized by linking $Zr_6O_4(OH)_4$ (or Zr_6) clusters with 1,3,5-benzenetricarboxylic acid (H_3BTC) ligands. Each Zr_6 cluster binds to six BTC linkers and possesses twelve vacant coordination sites for further ligand attachment, enhancing its versatility (Yang et al., 2021). The integration of biochar (BC) with MOFs combines their strengths, creating synergistic effects that increase active surface sites and significantly enhance pollutant adsorption capacities (Zhang et al., 2024b). Additionally, incorporating magnetic nanoparticles improves not only the adsorption capacity but also facilitates easy separation of the adsorbent from aqueous solutions (Zhang, 2024). Among magnetic nanoparticles, cobalt ferrite ($CoFe_2O_4$) is particularly noteworthy due to its reusability, abundance of active sites, cost-effective synthesis, strong magnetism, and widespread availability (Rabeie and Mahmoodi, 2024). $CoFe_2O_4$ exhibits a range of advantageous properties, including chemical and thermal stability, mechanical hardness, wear resistance, and electrical conductivity, along with multiple redox states (Salih et al., 2024). These attributes make $CoFe_2O_4$ a top choice as a magnetic adsorbent for efficiently removing organic pollutants from water (Chang et al., 2020; Zare et al., 2024).

This study developed biochar from pistachio shells, modified with magnetic nanoparticles $CoFe_2O_4$ and MOF-808, to create a magnetic composite (PSBC/$CoFe_2O_4$/MOF-808). The composite's effectiveness in removing methylene blue (MB) dye and diazinon (DA) pesticide from various water sources was investigated. Notably, this is the first study to utilize MOF-808-modified magnetic pistachio shell biochar for the removal of DA from water, as supported by previous literature. The magnetic composite was characterized using advanced analytical techniques, and the effects of key parameters such as pH, temperature, adsorbent dosage, pollutant concentration, and adsorption time on removal efficiency were systematically examined. Additionally, the study assessed the composite's performance in different water sources and conducted kinetic, thermodynamic, and isotherm analyses to provide deeper insights into the adsorption process.

2. Experimental section

2.1. Reagents and apparatus

Pistachio shells, an agricultural byproduct widely utilized for biochar production, were procured from local markets. Cobalt nitrate hexahydrate ($Co(NO_3)_2{\cdot}6H_2O$) was supplied by BioChem Chemopharma, while iron(III) chloride hexahydrate ($FeCl_3{\cdot}6H_2O$) and the pesticide diazinon (DA, λ_{max} = 247 nm) were obtained from Merck. Additional reagents, including formic acid (FA), zirconium chloride octahydrate ($ZrOCl_2{\cdot}8H_2O$), methylene blue dye (MB, MW = 319.85 g/mol, λ_{max} = 664 nm), and sodium hydroxide (NaOH), were purchased from Sigma-Aldrich. The ligand 1,3,5-benzenetricarboxylic acid (H_3BTC) was acquired from Aladdin Chemical Reagent Co., and N, N-dimethylformamide (DMF) was sourced from Macklin Biochemical Co. Deionized water was used consistently for solution preparation and washing throughout the experiments.

To examine the structural properties of the samples within the range of 5–70°, an X-ray diffraction (XRD) analysis was conducted using a Philips Xpert instrument with CuKα radiation (λ = 0.154 nm). Fourier-transform infrared spectroscopy (FTIR) was carried out with a Bruker Tensor-27 spectrophotometer, covering the range of 400–4000 cm^{-1}, to identify functional groups present on the sample surfaces. The specific surface area, pore volume, and average pore diameter were measured using nitrogen adsorption-desorption isotherms on a Belsorp Mini II instrument. Surface morphology, elemental composition, and distribution were analyzed using SEM and Mapping-EDX results obtained from a SEM-TESCAN MIRA3-FEG system. Raman spectroscopy, performed with a Bruker FRA 106/S spectrometer and a 532 nm laser, was used to study the graphitic structure of PSBC and PSBC/$CoFe_2O_4$/MOF-808 magnetic composite samples.

2.2. Synthesis of PSBC/$CoFe_2O_4$/MOF-808 magnetic composite

2.2.1. Synthesis of PSBC

To produce biochar from pistachio shells (PSBC), the shells were first thoroughly washed multiple times with deionized water and then dried completely for 24 h at 100 °C. Subsequently, 30 g of the dried pistachio shells were wrapped in thick aluminum foil and placed in a thermal furnace under a nitrogen atmosphere at 300 °C for 2 h, with a heating rate of 10 °C/min, to fully convert the shells into biochar (Daneshvar et al., 2024). After the heating process, the produced biochar was removed from the furnace and ground into powder using a ball mill for 4 h. The powdered biochar was then placed in a desiccator at room temperature to eliminate any residual moisture.

2.2.2. Synthesis of PSBC/$CoFe_2O_4$ magnetic composite

The PSBC/$CoFe_2O_4$ magnetic composite was synthesized using a chemical precipitation method, detailed as follows. An aqueous solution containing 0.1 mol/L of $Co(NO_3)_2{\cdot}6H_2O$ and 0.2 mol/L of $FeCl_3{\cdot}6H_2O$ was prepared. Two grams of PSBC were introduced into the solution and stirred for 30 min using a magnetic stirrer. The temperature was then increased to 85 °C, and the pH was adjusted to 10 by adding 10 mL of a 2 mol/L NaOH solution. The mixture was stirred for another 120 min. Afterward, the PSBC/$CoFe_2O_4$ magnetic composite was isolated from the

solution using a magnet, thoroughly washed with deionized water, and dried at 105 °C for 24 h to ensure complete drying.

2.2.3. Synthesis of MOF-808 and PSBC/$CoFe_2O_4$/MOF-808 magnetic composite

MOF-808 was synthesized via a hydrothermal method, as previously described in the literature (Su et al., 2022). Briefly, 0.97 g of $ZrOCl_2{\cdot}8H_2O$ were added to 25 mL of a DMF/FA solution in a 1:1 vol ratio and stirred magnetically for 30 min (Solution A). Simultaneously, 0.21 g of H_3BTC were dissolved in another 25 mL of a DMF/FA solution with the same ratio and stirred for 30 min until fully dissolved (Solution B). Solution A was then transferred to a stainless-steel Teflon autoclave, to which Solution B was added, and the mixture was stirred for an additional 10 min. The autoclave was sealed and heated in an oven at 120 °C for 48 h. After completing the hydrothermal process, it was allowed to cool to room temperature (25 ± 3 °C). The resulting white precipitate was then collected and washed several times with DMF and ethanol. The final white powder was dried in a vacuum oven at 80 °C for 24 h to produce MOF-808.

To synthesize the PSBC/$CoFe_2O_4$/MOF-808 magnetic composite, a mechanochemical method was employed. Specifically, 1 g of the PSBC/$CoFe_2O_4$ magnetic composite and 0.5 g of MOF-808 were mixed in a mortar without any solvent and ground together using a pestle for 30 min. During grinding, the color of the PSBC/$CoFe_2O_4$ composite changed from black to gray, indicating the incorporation of MOF-808 into its structure. After grinding, the PSBC/$CoFe_2O_4$/MOF-808 composite was washed with ethanol and acetone and dried for 24 h at 75 °C to ensure complete drying. The resulting composite was then stored at room temperature in moisture-resistant sealed glass containers and utilized as an effective and suitable adsorbent for removing MB and DA. Scheme 1 illustrates the synthesis process of the PSBC, PSBC/$CoFe_2O_4$, MOF-808, and PSBC/$CoFe_2O_4$/MOF-808 samples.

2.3. Adsorption study

The capability and efficiency of the PSBC/$CoFe_2O_4$/MOF-808 magnetic composite for adsorbing MB dye and DA pesticide were assessed in batch experiments conducted in 100 mL glass Erlenmeyer flasks. In each adsorption experiment with MB dye or DA pesticide, 50 mL of an aqueous solution containing specific concentrations of MB dye or DA pesticide was prepared. The pH of the solutions was set using 0.1 mol/L NaOH or HCl. After setting the initial pH, a measured amount of the PSBC/$CoFe_2O_4$/MOF-808 magnetic composite was added to the solution and stirred at 300 rpm for a set period. After the adsorption process, the magnetic composite was isolated, and the residual concentrations of MB dye and DA pesticide were measured via UV–vis spectrophotometry at their respective peak wavelengths of 664 nm and 274 nm. The elimination efficiency and adsorption capacity of the PSBC/$CoFe_2O_4$/MOF-808 composite for both contaminants were determined using Equations (1) and (2).

$$\text{Elimination (\%)} = 100 \times [(C_i - C_e)/C_i] \quad (1)$$

$$\text{Adsorption capacity (mg/g)} = (C_i - C_e) \times (V/D) \quad (2)$$

In this study, C_i and C_e set as the initial and final concentrations of MB dye and DA pesticide in the solution (mg/L), V refers to the volume of the solution used (L), and D denotes the dry weight of the PSBC/$CoFe_2O_4$/MOF-808 magnetic composite applied in each test (g/L). The parameters investigated as key factors affecting the adsorption process included pH (ranging from 2 to 10), temperature (25–55 °C), adsorbent mass (0.5–3 g/L), initial pollutant concentrations (5–40 mg/L), and contact time (5–140 min). Furthermore, the adsorption kinetics (examining models such as pseudo-first-order, pseudo-second-order, Elovich, and intraparticle diffusion), thermodynamics (enthalpy, entropy, and Gibbs free energy), and isotherms (Langmuir, Freundlich, and Dubinin-Radushkevich) were analyzed based on the effects of time, temperature, and pollutant content on the removal efficiency.

2.4. Practical applications and reusability assessment

The performance of the PSBC/$CoFe_2O_4$/MOF-808 composite in removing MB and DA from various water sources—including tap, well, distilled, mineral, and river water—was assessed under specific conditions: initial pH levels of 9 and 6, adsorbent dosages of 1 g/L and 1.5 g/L, a temperature of 55 °C, an initial pollutant concentration of 10 mg/L, and adsorption durations of 60 and 80 min.

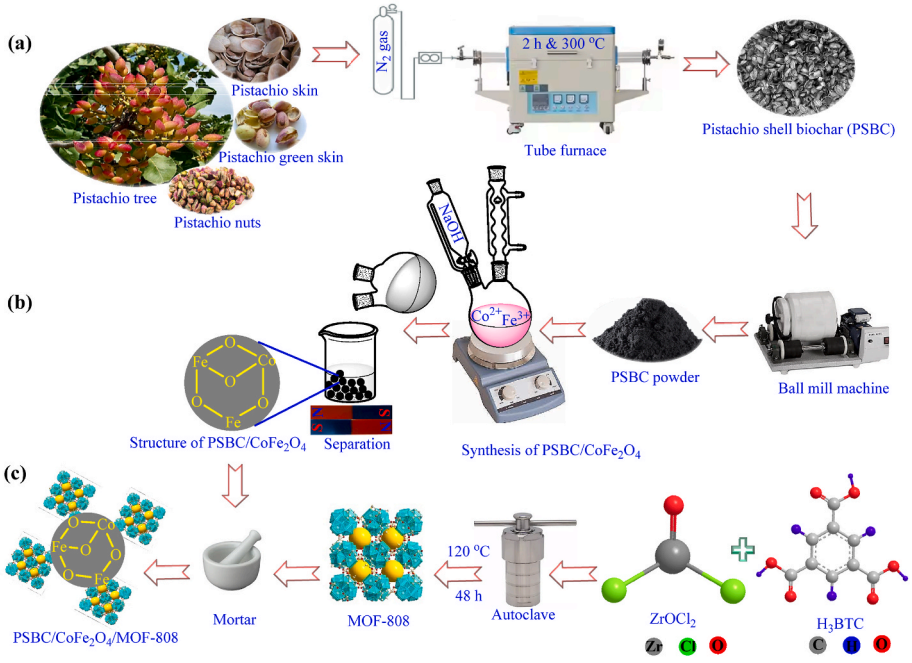

Scheme 1. Overview of the synthesis procedure: **(a)** PSBC, **(b)** PSBC/$CoFe_2O_4$, **(c)** MOF-808, and PSBC/$CoFe_2O_4$/MOF-808. The MOF-808 structure was sourced from the website 'https://shop.aminbic.ir/product/mof-808/'.

To regenerate and reuse the PSBC/$CoFe_2O_4$/MOF-808 composite for MB and DA removal, solutions of DMF/ethanol (Moradnejati et al., 2024) and 0.1 mol/L NaOH were used. After adsorbing MB and DA, the composite was separated from the water with a magnet and immersed in 50 mL of the DMF/ethanol and NaOH solutions for 90 min. Subsequently, the adsorbent was rinsed thoroughly with deionized water, dried at 105 °C for 120 min, and then reused in the adsorption process.

3. Results and discussion

3.1. Properties of the adsorbent

3.1.1. FTIR and XRD analysis

FTIR spectral analysis was performed to identify and explore the functional groups present in the PSBC, the PSBC/$CoFe_2O_4$ magnetic composite, and the PSBC/$CoFe_2O_4$/MOF-808 magnetic composite. The findings are illustrated in Fig. 1a–c. In these sample structures, absorption peaks were detected within the spans of 3425–3437 cm^{-1} and 2856–2964 cm^{-1}, corresponding to -OH and C-H functional groups, respectively (Yu et al., 2024). The PSBC sample also showed additional absorption peaks at 1627, 1521, 1458, 1000–1200, 873, 619, and 572 cm^{-1}, which were linked to C=C/C-O stretching vibrations (Jalayeri and Pepe, 2019), C=O groups in aromatic rings (Usman et al., 2015), C=C vibrations (Wang et al., 2024c), N=C=O stretching vibrations (Hassaan et al., 2024; Gong et al., 2024), hydroxyl/C-O groups (Del Pozo et al., 2022), aromatic C-H vibrations (Lee JeChan et al., 2017; Kopp Alves et al., 2024), aromatic ring vibrations (Singh et al., 2021), and C-H/C-C functional groups (Adhikari et al., 2024; Liu et al., 2023). Upon amendment of the PSBC sample with $CoFe_2O_4$ (PSBC/$CoFe_2O_4$), alterations in the intensity and position of functional groups were seen, likely due to interactions with the nanoparticles. Particularly, the PSBC/$CoFe_2O_4$ composite displayed a distinct absorption peak at 580 cm^{-1}, which was absent in the PSBC sample. This peak is associated with the stretching vibrations of metal ions in tetrahedral (Fe-O-Co) configurations (Lakshmigandhan et al., 2024), indicating successful nanoparticle integration. The FTIR spectrum of the PSBC/$CoFe_2O_4$/MOF-808 magnetic composite showed significant shifts in the intensity and location of functional groups in the 700–1700 cm^{-1} range, likely due to interactions between MOF-808 and PSBC/$CoFe_2O_4$. For instance, new peaks were observed at 1612–1616 cm^{-1} and 1384–1448 cm^{-1}, corresponding to Zr-COOH deprotonation and Zr-OH vibrations, respectively (Huang et al., 2024b). Moreover, the absorption peak at 1421 cm^{-1} in the PSBC/$CoFe_2O_4$ composite shifted to 1448 cm^{-1} after incorporating MOF-808, likely due to interactions involving the C=C vibrations in the aromatic ligands used to synthesize MOF-808 (Dashtipour et al., 2024). Furthermore, new absorption peaks were observed at 1242, 1180, 1010–1100, 742, and 651 cm^{-1}, attributed to C-O vibrations (Saeed et al., 2024), C=O vibrations (Ghasemzadeh and Akhbari, 2025; Liu et al., 2018), -OH in Zr_6 clusters (Wang et al., 2024b; Meng et al., 2023), Zr-O bond, and Zr-O-Zr connections (Kazemi et al., 2024; Su et al., 2024b).

X-ray diffraction (XRD) test was done to examine the crystalline and amorphous structure of PSBC, as well as the formation of $CoFe_2O_4$ magnetic nanoparticles and MOF-808 within the PSBC matrix, with the results shown in Fig. 1d. The PSBC sample exhibited two broad peaks at 15–30° and 40–45°, corresponding to the (002) and (100) crystalline phases associated with the graphitic and disordered graphitic planes in the PSBC structure (Al-Sareji et al., 2024). After the PSBC was modified

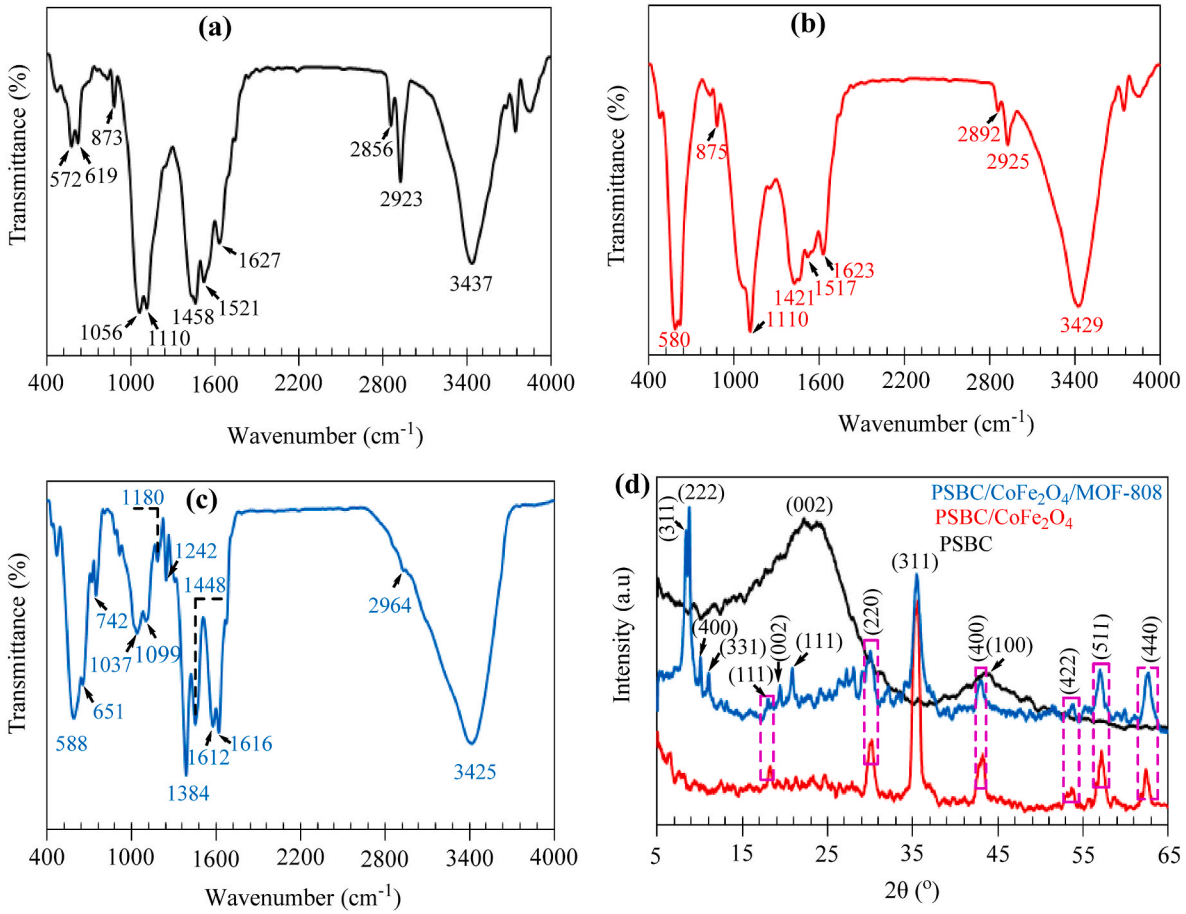

Fig. 1. FTIR spectra for samples **(a)** PSBC, **(b)** PSBC/$CoFe_2O_4$ magnetic composite, and **(c)** PSBC/$CoFe_2O_4$/MOF-808 magnetic composite; **(d)** XRD spectrum presented for the specified samples.

with $CoFe_2O_4$ magnetic nanoparticles (PSBC/$CoFe_2O_4$), significant structural changes were observed, including new peaks of varying intensities, suggesting the growth of $CoFe_2O_4$ magnetic particles. In the PSBC/$CoFe_2O_4$ sample structure, new peaks appeared at 18.24°, 30.14°, 35.49°, 43.18°, 53.60°, 57.06°, and 62.34°, corresponding to the crystalline phases (111), (220), (311), (400), (422), (511), and (440) in the structure of the PSBC/$CoFe_2O_4$ magnetic nanoparticles (Dong et al., 2016; Khanahmadi and Masoudpanah, 2024). Notably, the diffraction peaks observed in the PSBC/$CoFe_2O_4$ structure align with the inverse cubic spinel structure of $CoFe_2O_4$ with space group Fd-3m (Huerta-Flores et al., 2024), suggesting that $CoFe_2O_4$ crystals have successfully grown and formed within the PSBC structure. Following the refinement of PSBC/$CoFe_2O_4$ with MOF-808, shifts in the intensity and position of peaks within PSBC/$CoFe_2O_4$ were observed, along with the appearance of new peaks in the 2θ value of 5–30°, likely indicating the formation of MOF-808 particles and crystalline phases. In the XRD spectrum for the PSBC/$CoFe_2O_4$/MOF-808 magnetic composite, peaks were detected at 2θ values of 8.36°, 8.74°, 10.10°, and 11.06°, corresponding to the crystalline planes (311), (222), (400), and (331) present in MOF-808 (Menezes et al., 2025; Bao et al., 2025). Additionally, other lower intensity peaks were identified at 19.40° and 20.82°, which correspond to the crystalline planes (002) and (111) in the MOF-808 structure (Chen et al., 2024), indicating that the crystalline planes of MOF-808 have grown well and have been successfully incorporated into the PSBC/$CoFe_2O_4$/MOF-808 magnetic composite structure.

3.1.2. Raman and VSM analysis

Raman spectroscopy is currently one of the most effective appraoches for examining the structure of carbon-based materials (Makowska and Dziosa, 2024), as it provides insights into the defects within the carbon material and its crystalline or amorphous nature. The Raman spectra of PSBC and the PSBC/$CoFe_2O_4$/MOF-808 magnetic composite were analyzed over the range of 70–2000 cm^{-1}, with the results displayed in Fig. 2a. The findings show two prominent peaks at 1338.944 cm^{-1} and 1592.348 cm^{-1} in the PSBC sample, corresponding to the disordered crystal structure (D band) and the ordered crystalline structure (G band), respectively (Suratman et al., 2024; Ren et al., 2024). The D band reflects defects, structural disruptions, and functional groups within the material, with its intensity being related to the number of SP^3 carbon atoms and the number of defects present. Meanwhile, the G band arises from the stretching vibrations of SP^2 carbon atoms, signifying graphitic carbon (Alonso-Gómez et al., 2024; He et al., 2024). Following the formation of the PSBC/$CoFe_2O_4$/MOF-808 magnetic composite, the D and G band peaks shifted to 1342.838 cm^{-1} and 1590.470 cm^{-1}, respectively, which may be due to interactions between the components of the composite.

In addition to the D and G bands, new peaks appeared between 250 and 660 cm^{-1} in the PSBC/$CoFe_2O_4$/MOF-808 composite, corresponding to the Raman vibration modes Eg, T_2g, and A_1g, which are associated with $CoFe_2O_4$ magnetic nanoparticles (Palsaniya et al., 2024), indicating the presence of Raman-active modes of $CoFe_2O_4$ with a spinel structure (Fd-3m) (Abdel-Fattah et al., 2024), aligning with the XRD findings. Raman spectroscopy was also employed to evaluate the defects and the degree of crystallinity in the PSBC and PSBC/$CoFe_2O_4$/MOF-808 magnetic composite samples, with the degree of defectiveness quantified by the ratio of I_D to I_G (I_D/I_G). The I_D/I_G ratio for PSBC was determined to be 0.967, while for the PSBC/$CoFe_2O_4$/MOF-808 magnetic composite, it was 0.941. The lower I_D/I_G ratio in the PSBC/$CoFe_2O_4$/MOF-808 composite suggests a more ordered graphitic structure, fewer defects, and fewer structural irregularities, along with a higher number of oxygen-containing groups (Revathi et al., 2024), implying that the reduction in defects may be due to the integration of $CoFe_2O_4$ nanoparticles and MOF-808 into the pores and surface of PSBC (Wang et al., 2024d; Alharthi et al., 2024).

The magnetic properties of the PSBC/$CoFe_2O_4$/MOF-808 magnetic composite are critical for its recovery and reuse as an adsorbent, which can reduce the overall process costs. To assess its magnetic characteristics, vibrating sample magnetometry (VSM) was conducted in the value of ±8000 Oe, with the outcomes shown in Fig. 2b. The saturation magnetization of the PSBC/$CoFe_2O_4$/MOF-808 magnetic composite was found to be 19.65 emu/g, which is lower than the previously stated saturation magnetization for $CoFe_2O_4$ (Yadav et al., 2024; Bhat et al., 2024). The reduction in magnetization may be due to several factors, including the presence of non-magnetic components like PSM and MOF-808 (Viante et al., 2018), cation distribution within the spinel structure, an increased surface-to-volume ratio, random spin orientation at the surface, the formation of a dead magnetic layer (Ajami et al., 2024), surface defects, and the average particle size (Heydari et al., 2024).

In the analysis of magnetic properties, the remanence ratio (R), described as the ratio of remanent magnetization (M_r) to saturation magnetization (M_s) ($R = M_r/M_s$), is an essential parameter. According to Stoner-Wohlfarth theory, the ratio can take two distinct values: 0.8 for cubic anisotropy and 0.5 for uniaxial anisotropy (Bhat et al., 2024). The R value for the PSBC/$CoFe_2O_4$/MOF-808 magnetic composite was determined to be 0.183, indicating that the $CoFe_2O_4$ magnetic particles within the composite exhibit axial anisotropy and interact with one another through magnetic interactions (Mohan et al., 2024). The coercivity (Hc) for the PSBC/$CoFe_2O_4$/MOF-808 magnetic composite was measured to be 171 Oe, with this low Hc value suggesting that the magnetic properties of the material are approaching a superparamagnetic state (Kapur et al., 2024).

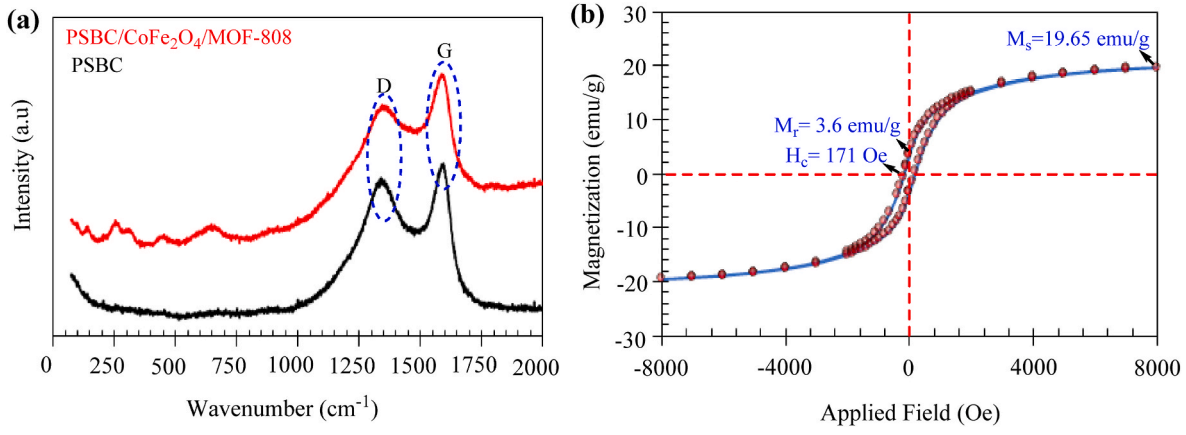

Fig. 2. **(a)** Raman spectra for PSBC and PSBC/$CoFe_2O_4$/MOF-808, **(b)** VSM diagram for PSBC/$CoFe_2O_4$/MOF-808.

3.1.3. BET analysis

The N_2 adsorption-desorption (N_2 ads-des) isotherms for the PSBC sample and the PSBC/$CoFe_2O_4$/MOF-808 magnetic composite, along with their pore size distributions, are presented in Fig. 3a and b. The N_2 ads-des isotherm for the PSBC sample aligns with a type IV isotherm, as defined by the International Union of Pure and Applied Chemistry (IUPAC), which is typical of mesoporous materials (Gao et al., 2021). After modifying the PSBC sample with $CoFe_2O_4$ magnetic nanoparticles and MOF-808, the isotherm shifted to a combination of type I and type IV isotherms. This indicates that MOF-808 was successfully incorporated into the PSBC/$CoFe_2O_4$/MOF-808 magnetic composite structure. The presence of the type I isotherm and the rapid N_2 adsorption at P/P0 < 0.1 suggests a high micropore content in the PSBC/$CoFe_2O_4$/MOF-808 magnetic composite (Fu et al., 2022). Moreover, the absence of significant hysteresis in the N_2 ads-des isotherm for the composite suggests a lower amount of mesopores in the structure (Amedi and Aghajani, 2017). The specific areas of PSBC and PSBC/$CoFe_2O_4$/MOF-808 were measured to be 17.504 m^2/g and 151.53 m^2/g, respectively, indicating that the addition of $CoFe_2O_4$ magnetic nanoparticles and MOF-808 increased the surface area. It is worth noting that the increase in specific active surface area by placing $CoFe_2O_4$ magnetic nanoparticles and MOF-808 in the PSBC structure can be attributed to the presence of small-sized particles in the PSBC structure, the opening of the internal porosity of the PSBC structure, and the creation of new pores and gaps in the PSBC structure (Amusat et al., 2022). Additionally, the average pore diameters of PSBC and the PSBC/$CoFe_2O_4$/MOF-808 magnetic composite were found to be 6.461 nm and 2.518 nm, respectively, which are within the 2–50 nm span, confirming their mesoporous structure (Damiri et al., 2020). The pore volumes for PSBC and the PSBC/$CoFe_2O_4$/MOF-808 magnetic composite were determined to be 0.028 cm^3/g and 0.095 cm^3/g, respectively, showing that the modification also enhanced pore volume.

3.1.4. SEM, EDX, and mapping analysis

SEM and EDX analyses were conducted to examine the elemental composition, surface features, and morphology of the PSBC and PSBC/$CoFe_2O_4$/MOF-808 magnetic composite samples at a scale of 1–2 μm, with the findings shown in Fig. 4. SEM images of the PSBC sample revealed large pores on its surface (Fig. 4a and b), which could provide ideal sites for pollutant adsorption and the deposition of $CoFe_2O_4$ and MOF-808 magnetic nanoparticles. The EDX analysis further confirmed that the PSBC structure contained only carbon (77.32 W%) and oxygen (22.68 W%), without any other impurities, indicating the successful synthesis of the carbon structure (Fig. 4c). Significant alterations in the surface properties were observed following the modification of PSBC with $CoFe_2O_4$ and MOF-808. Small particles with nearly spherical morphologies covered the surface and pores (Fig. 4d and e), indicating the successful deposition of $CoFe_2O_4$ and MOF-808 nanoparticles. In the SEM images of the PSBC/$CoFe_2O_4$/MOF-808 magnetic composite, the aggregation of $CoFe_2O_4$ and MOF-808 nanoparticles on the PSBC surface was observed, which could be attributed to magnetostatic interactions based on the VSM results (Mohan et al., 2024). The EDX analysis confirmed the presence of carbon (34.74 W%), oxygen (29.34 W%), zirconium (16.57 W%), cobalt (4.45 W%), and iron (14.90 W%) in the structure of the PSBC/$CoFe_2O_4$/MOF-808 magnetic composite (Fig. 4f), indicating the successful integration of CoFe2O4 and MOF-808 nanoparticles into the PSBC structure through chemical precipitation and ball milling. Fig. 4g presents the mapping analysis for the PSBC/$CoFe_2O_4$/-MOF-808 composite, showing the distribution of elements confirmed by the EDX analysis, and further validating the successful synthesis of the composite. It is noteworthy that the SEM results align well with the BET data, both indicating that the average pore diameter in the PSBC structure is larger compared to PSBC/$CoFe_2O_4$/MOF-808. This reduction in pore size is likely due to the deposition and growth of $CoFe_2O_4$ and MOF-808 nanoparticles within the PSBC pores.

3.2. Effect of key parameters on the adsorption

One of the most critical factors influencing the adsorption process is pH, as it affects the adsorption efficiency by influencing the surface charge of the adsorbent and the ionization of the adsorbed molecules (Fang et al., 2024). As depicted in Fig. 5a, the adsorption efficiency of MB increased from 33.54% to 94.93% as the pH was raised from 2 to 10 using the PSBC/$CoFe_2O_4$/MOF-808 magnetic composite. In contrast, the adsorption of DA pesticide increased from 42.78% at pH 2–90.54% at pH 6, but then decreased. This behavior for both MB dye and DA pesticide can be explained through the pHpzc results depicted in Fig. 5b. The pHpzc values for PSBC and PSBC/$CoFe_2O_4$/MOF-808 were determined to be 6.67 and 6.4, respectively, indicating that the samples exhibit cationic surface charges at pH < pHpzc and anionic surface charges at pH > pHpzc. The increase in DA pesticide removal efficiency as pH increases from 2 to 6 can be explained by the transformation of DA pesticide (pKa = 2.6) into an anionic form at pH > 2.6 (Moussavi et al., 2013), creating an electrostatic attraction between the anionic DA and the positively charged adsorbent surface, thereby improving adsorption efficiency. When pH < pHpzc, excess H^+ ions compete with the cationic groups of the MB dye for adsorptive sites, leading to protonation of the adsorbent's active sites and a decrease in removal efficiency (Chen et al., 2021), due to electrostatic repulsion between the positively charged adsorbent surface and the cationic MB molecule. At pH > pHpzc, the

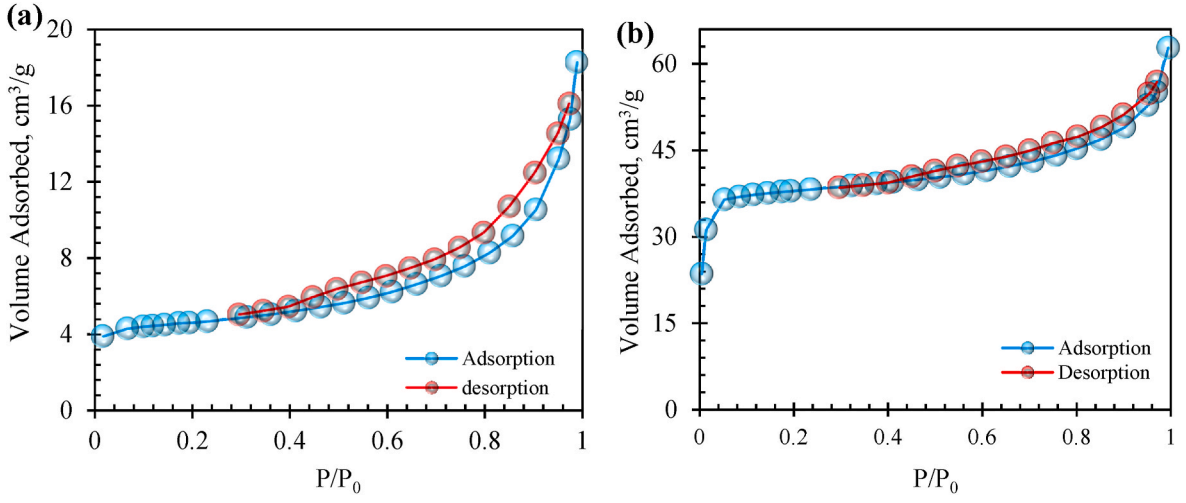

Fig. 3. – N_2 ads-des isotherms for examining the area, pore volume, and average pore diameter in the structure of **(a)** PSBC and **(b)** PSBC/$CoFe_2O_4$/MOF-808.

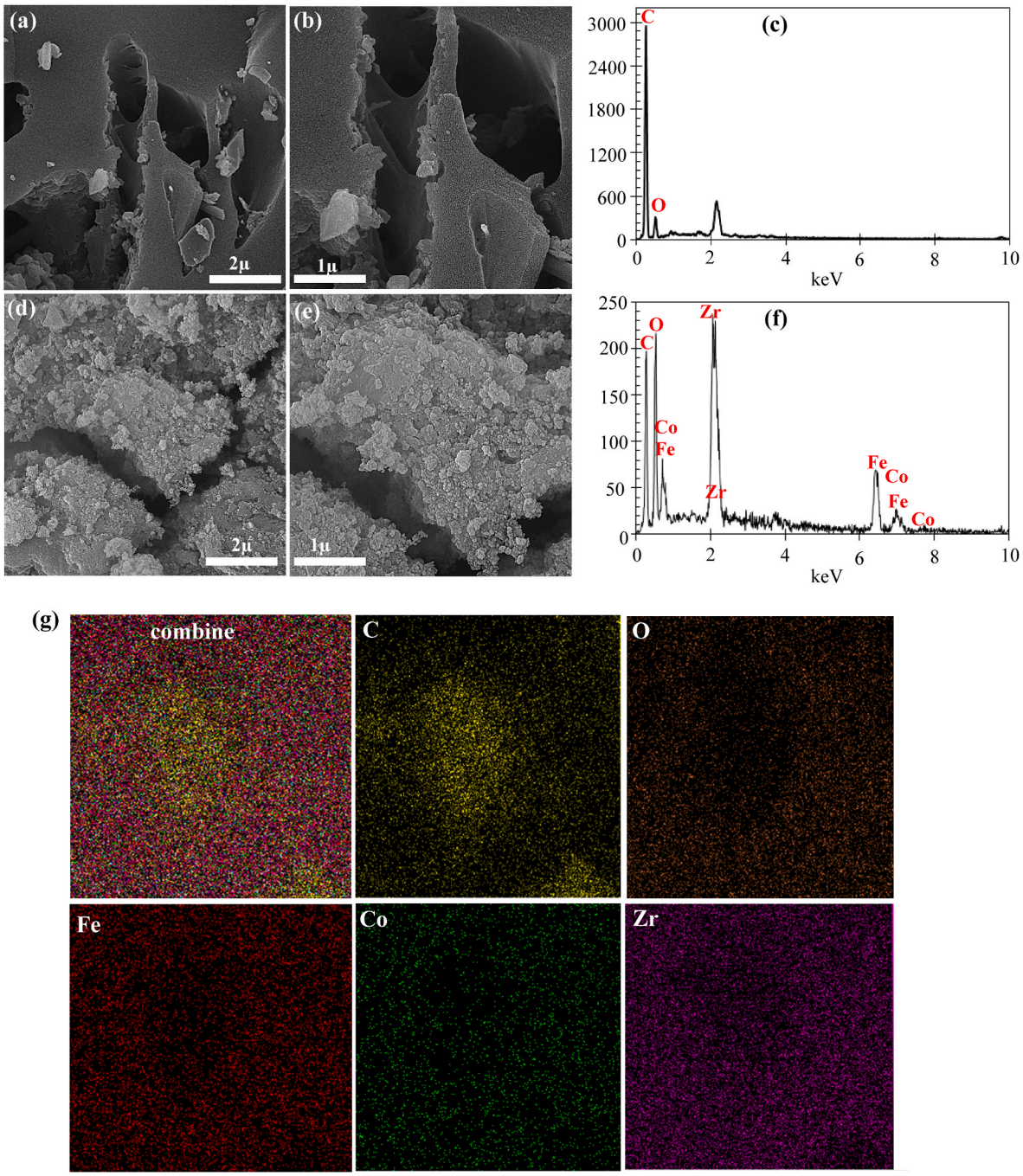

Fig. 4. – SEM-EDX test with magnifications of 1–2 μm for: **(a–c)** PSBC and **(d–f)** PSBC/$CoFe_2O_4$/MOF-808, and **(g)** mapping images of the elements present in the structure of PSBC/$CoFe_2O_4$/MOF-808.

surface of the PSBC and PSBC/$CoFe_2O_4$/MOF-808 samples becomes more negatively charged, enhancing electrostatic attraction and improving the removal of the cationic MB dye (Li et al., 2021). However, while a higher pH improves MB dye adsorption, it hinders DA pesticide adsorption, as the increased pH causes greater dissociation of the DA pesticide, increasing its negative charge (Hassan et al., 2017), which leads to electrostatic repulsion between the negatively charged adsorbent and the DA pesticide, thereby reducing DA adsorption.

In this study, the adsorbent dosage of the PSBC/$CoFe_2O_4$/MOF-808 magnetic composite was tested for the removal of MB and DA. As shown in Fig. 5c, increasing the composite dosage from 0.5 to 1 and 1.5 g/L improved the adsorption efficiency from 59.43% to 43.28%–94.82% and 94.55% for MB and DA, respectively, mainly due to the greater surface area and higher number of available adsorption sites at higher dosages (Chen et al., 2020; Murthy et al., 2020). However, when the adsorbent mass increased from 0.5 to 3 g/L, the adsorption capacity for MB and DA decreased from 11.886 mg/g and 8.656 mg/g to 3.202 mg/g and 3.172 mg/g, respectively (Fig. 5d). This can be explained by the saturation of the adsorbent's active sites by MB and DA molecules, requiring more energy for additional adsorption, thus reducing adsorption capacity (Qin et al., 2024).

The temperature was studied for the adsorption of MB and DA, with the results shown in Fig. 6a. Increasing the temperature from 25 to 55 °C improved the abatement of MB and DA using the magnetic composite from 94.82% to 94.55%–99.24% and 98.81%, respectively, confirming the endothermic nature of the adsorption. The enhanced adsorption

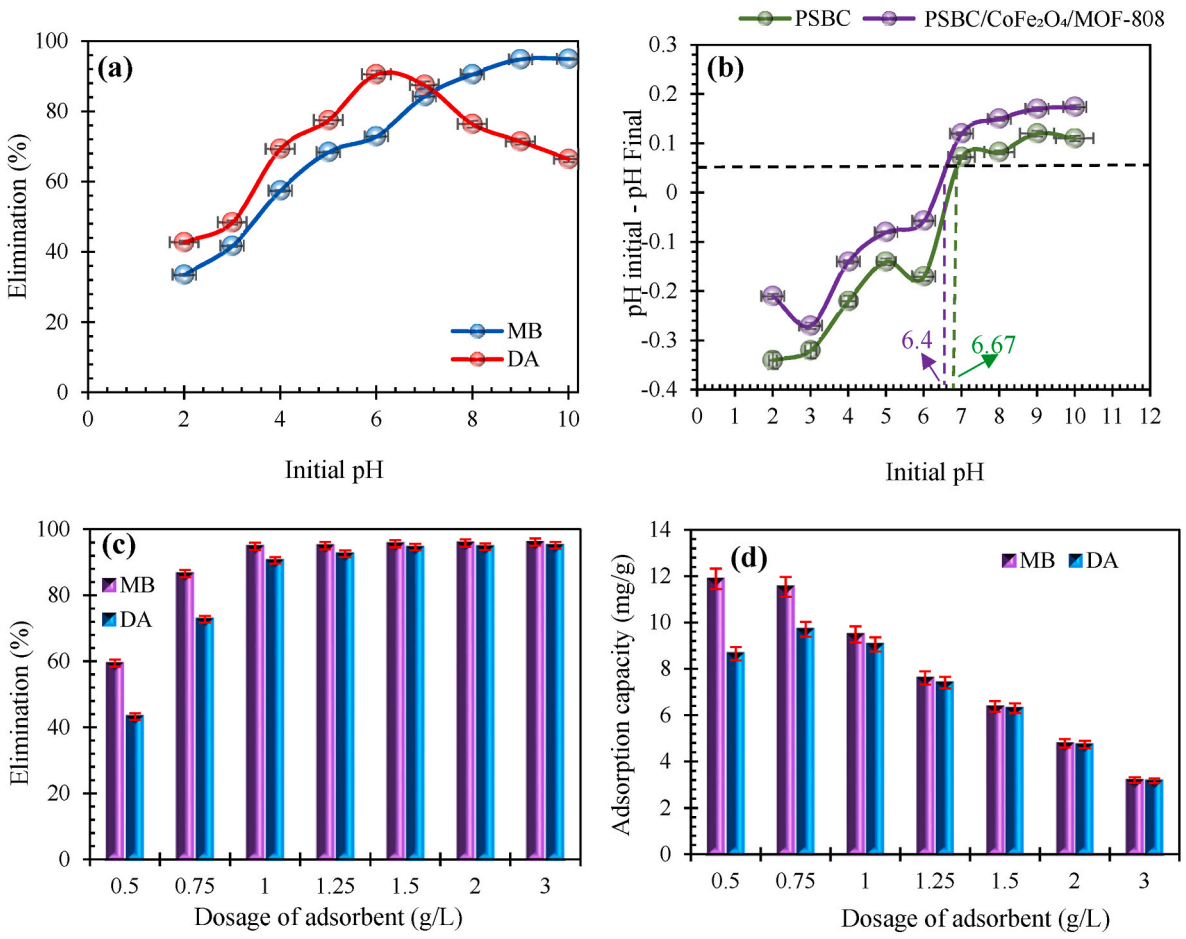

Fig. 5. **(a)** The impact of pH (temperature 25 °C, time 80 min, adsorbent dosage 1 g/L, pollutant concentration 10 mg/L), **(b)** pH initial - pH Final versus Initial pH for determining pHpzc, **(c, d)** The impact of adsorbent mass on the pollutant removal and adsorption capacity (temperature 25 °C, time 80 min, pH for MB and DA adsorption set at 9 and 6, respectively, pollutant concentration 10 mg/L).

performance with higher temperatures can be attributed to factors like reduced viscosity of the aqueous solution, increased kinetic energy (Moussavi et al., 2013; Hameed et al., 2024), improved molecular diffusion of MB and DA through the external boundary layer of the PSBC/$CoFe_2O_4$/MOF-808 magnetic composite (Chaima et al., 2024), greater mobility of MB and DA molecules in the solution, leading to more frequent collisions with active adsorption sites, expansion of the adsorbent's pores due to thermal expansion, and a rise in the quantity of adsorptive sites (Su et al., 2024c).

A crucial aspect of efficient adsorption processes is rapid adsorption, which can greatly impact the practical use of the adsorbent (El-Desouky et al., 2024). The influence of adsorption time on the removal efficiency of MB dye and DA pesticide was explored over intervals of 5–140 min, with initial pH values of 9 and 6 for MB dye and DA pesticide, respectively. The experiments were conducted using adsorbent masses of 1 and 1.5 g/L for MB and DA and initial pollutant concentrations of 10 mg/L (Fig. 6b). The experimental outcomes indicated that the adsorption efficiency for MB and DA using PSBC/$CoFe_2O_4$/MOF-808 increased from 54.43% to 41.42%–99.17% and 98.81% as the contact time increased from 5 to 60 and 80 min, respectively. As illustrated in Fig. 6b, the adsorption rate was more rapid during the initial stages due to a higher availability of unsaturated active sites. The improved efficiency with extended contact times can be attributed to the adequate time allowed for effective interactions between MB and DA molecules and the active adsorption sites (Hashemkhani et al., 2022). However, after 60 and 80 min, no significant increase in removal efficiency was seen, suggesting that the active sites had reached saturation (Shukla et al., 2024; Farmany et al., 2016).

The effects of initial pollutant concentrations for MB and DA were examined in the range of 5–40 mg/L, with results presented in Fig. 6c and d. As represented in Fig. 6c, rising the initial concentrations of MB and DA from 5 to 40 mg/L led to a decline in removal outcome from 99.32% to 99.14%–84.32% and 78.43%, respectively. This reduction can be attributed to the saturation of the adsorbent's pores, limited access to remaining pores (Bellaj et al., 2024; Yildiz, 2024), and saturation of surface and active sites, resulting in fewer available adsorption sites (Behera et al., 2024). Nevertheless, despite the decrease in removal efficiency, the experimental data in Fig. 6d indicate that higher pollutant concentrations resulted in an increase in adsorption capacity, aligning with previous studies (Meskel et al., 2024; Li et al., 2024; Cai et al., 2024).

3.3. Thermodynamic and kinetic study

To assess the impact of temperature on the removal efficiency of MB and DA with the PSBC/$CoFe_2O_4$/MOF-808 magnetic composite, as well as to analyze the spontaneity and thermal nature of the process, key thermodynamic parameters including Gibbs free energy (ΔG), enthalpy (ΔH), and entropy (ΔS) were examined. The calculations for these thermodynamic parameters were performed using Equations (3) and (4) (Fan et al., 2024b):

$$\Delta G = -RT\ln k_D \quad (3)$$

$$\ln k_D = -\frac{\Delta H}{RT} + \frac{\Delta S}{R} \quad (4)$$

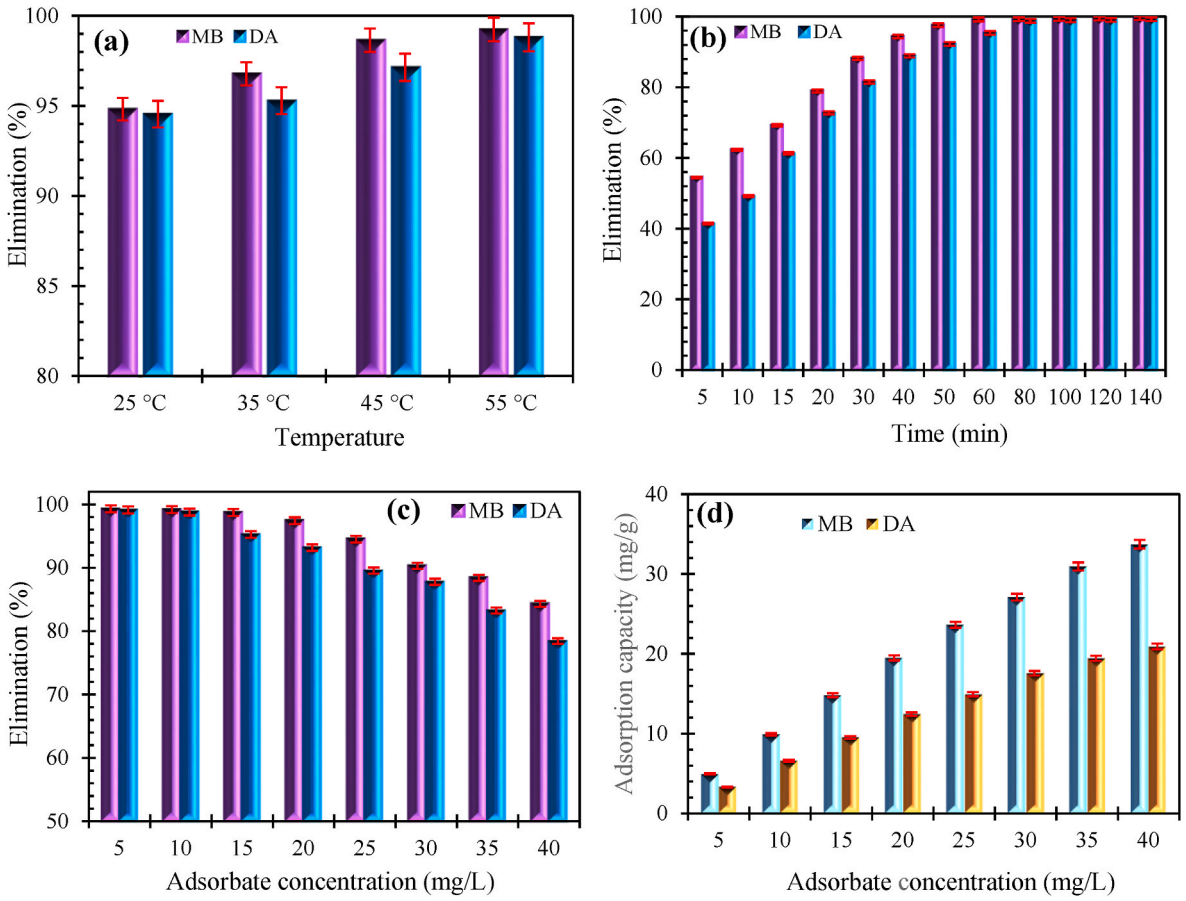

Fig. 6. **(a)** The effect of temperature on the removal efficiency of the pollutants (pH for MB dye and DA pesticide removal set at 9 and 6, respectively, adsorbent dosage for MB and DA removal at 1 and 1.5 g/L, time 80 min, initial pollutant content 10 mg/L), **(b)** The effect of contact time on removal efficiency (pH for MB and DA removal set at 9 and 6, respectively, adsorbent dosage for MB and DA removal at 1 and 1.5 g/L, temperature 55 °C, initial pollutant concentration 10 mg/L), **(c, d)** The effect of pollutants quantity on their removal and adsorption capacity adsorbate (pH for MB and DA removal set at 9 and 6, respectively, adsorbent dosage for MB and DA removal at 1 and 1.5 g/L, temperature 55 °C, time for MB and DA removal set at 60 and 80 min, respectively).

Here, 'R' denotes the universal gas constant (8.314 J/mol·K), 'T' represents the system temperature (K), and 'k_D' signifies the equilibrium constant. The linear plot of ln(kD) versus 1/T, utilized to calculate the ΔH and ΔS values, is illustrated in Fig. 7a. The thermodynamic values for the adsorption processes of MB and DA with the PSBC/$CoFe_2O_4$/MOF-808 magnetic composite are summarized in Table 1. The results indicate that the ΔG values for the adsorption of MB and DA within the 25–55 °C temperature range are negative, confirming the feasibility and spontaneity of the adsorption process (Zain et al., 2024). Furthermore, ΔG values become increasingly negative with higher temperatures, suggesting that adsorption efficiency is temperature-dependent. Notably, the ΔG value for MB removal is more negative than that for DA, indicating a higher affinity of the PSBC/$CoFe_2O_4$/MOF-808 magnetic composite for MB. The ΔH values for the adsorption of MB and DA were calculated as 55.051 and 42.028 kJ/mol, respectively, confirming the endothermic nature of the process (Behera et al., 2024). In addition, the ΔH value for the adsorption of the mentioned pollutants was determined to be less than 84 kJ/mol, indicating that the adsorption process under the conditions performed is physical (Ehsani et al., 2023). Additionally, the ΔS values for the adsorption of MB and DA were found to be 0.208 and 0.163 kJ/mol, respectively, indicating structural changes in both the adsorbent and the pollutants (Zain et al., 2024; Altıntıg et al., 2017) and an increase in disorder at the interface between the water and the composite (Ouaddari et al., 2024). This increase in disorder can also be linked to the release of water molecules, which facilitates molecular exchange between MB and DA and the functional groups on the surface of the PSBC/$CoFe_2O_4$/MOF-808 magnetic composite (Değermenci et al., 2019).

To investigate the fundamental mechanisms of the adsorption process and assess the adsorption rate for commercial unit design, a more detailed study was conducted. The following kinetic models were evaluated to better understand the kinetic behavior of the process (Equations (5)–(8)).

$$\text{Pseudo first order, } q_t = q_{e.cal} \times (1 - \exp(-k_1 \times t)) \quad (5)$$

$$\text{Pseudo secend order, } q_t = \frac{k_2 \times q_{e.cal}^2 \times t}{1 + k_2 \times q_{e.cal} \times t} \quad (6)$$

$$\text{Elovich : } q_t = \frac{1}{\beta}\ln(1 + \alpha\beta\, t) \quad (7)$$

$$\text{Intra particle diffusion, } q_t = k_{int} \times t^{0.5} + g \quad (8)$$

In this context, 'q_t' represents the uptake capacity at time t (mg/g), while '$q_{e.cal}$' indicates the calculated adsorption capacity (mg/g). 'k_1' is the adsorption rate constant for the pseudo-first-order (PFO) model (1/min), and 'k_2' is the adsorption rate constant for the pseudo-second-order (PSO) model (g/mg·min). Additionally, 'k_{int}' denotes the intra-particle diffusion (IPD) rate constant (mg/g·$min^{1/2}$), 'α' (mg/g·min) represents the initial adsorption rate, 'β' (g/mg) is the Elovich model constant, and 'g' corresponds to the intercept of the intra-particle diffusion plot.

The nonlinear relationships of the kinetic models for the adsorption of pollutants using the PSBC/$CoFe_2O_4$/MOF-808 magnetic composite are illustrated in Fig. 7b and c, respectively. The constants and variables

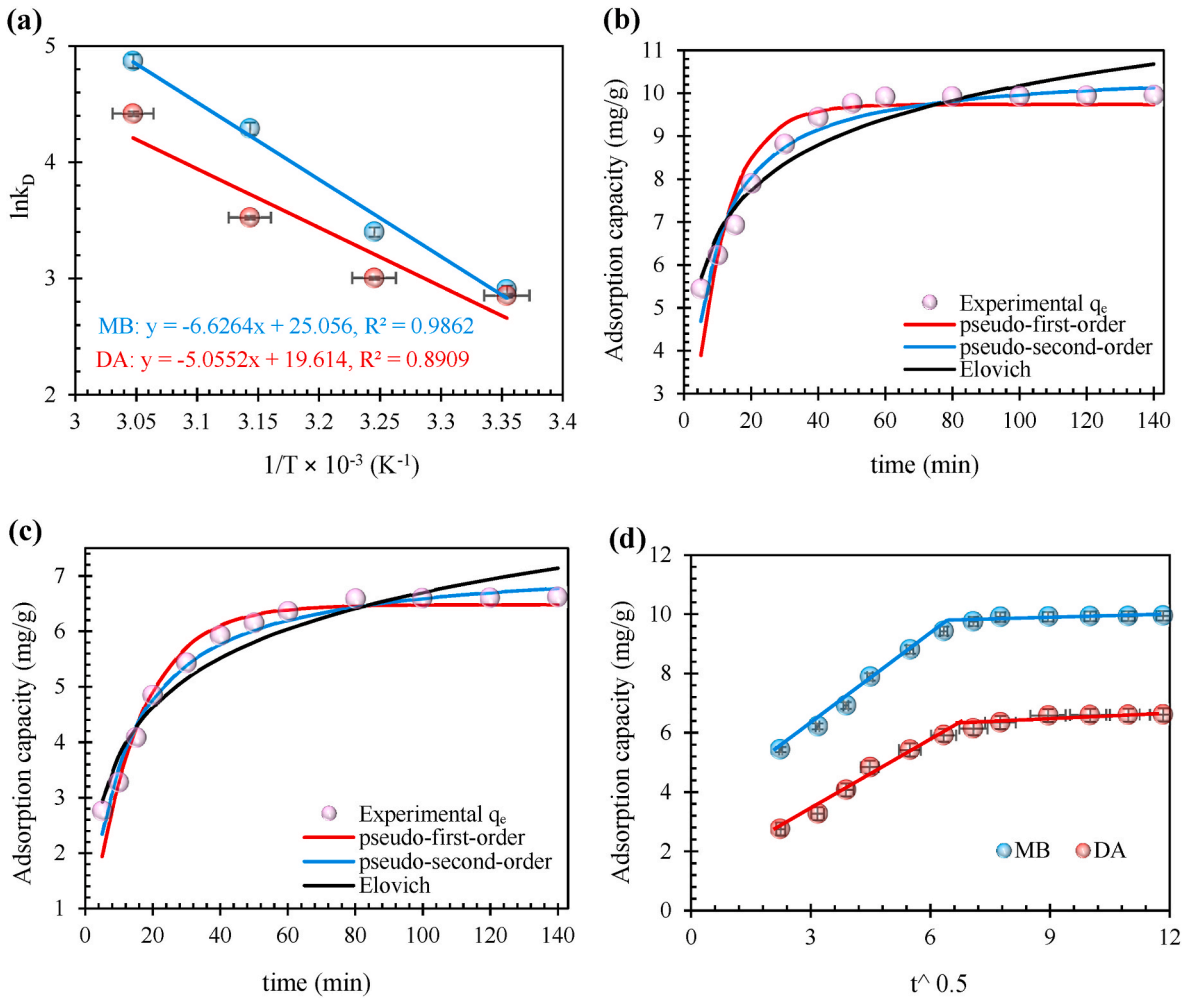

Fig. 7. **(a)** Linear correlation of lnk_D versus 1/T for determining thermodynamic values; nonlinear relationships of the kinetic models for the removal of **(b)** MB and **(c)** DA; **(d)** linear correlation of the intraparticle diffusion model for the removal of MB and DA.

Table 1
Determined thermodynamic values for the removal process of MB and DA using the PSBC/$CoFe_2O_4$/MOF-808.

Adsorbate	T (°C)	ΔG (kJ/mol)	ΔH (kJ/mol)	ΔS (kJ/mol)
MB	25	−7.206	55.091	0.208
	35	−8.718		
	45	−11.351		
	55	−13.291		
AD	25	−7.073	42.028	0.163
	35	−7.698		
	45	−9.324		
	55	−12.056		

derived from these kinetic models are summarized in Table 2. According to the results, the pseudo-second-order kinetic model displays higher R^2 values and lower RMSE values compared to both the pseudo-first-order and Elovich models, indicating that the kinetic data conforms to the pseudo-second-order model. This alignment of the kinetic data with the pseudo-second-order model suggests that chemical adsorption (the rate-limiting step) plays a significant and effective role in the removal of the specified pollutants (Liu et al., 2025), with the adsorption rate and speed depending on the active sites available in the PSBC/$CoFe_2O_4$/MOF-808 magnetic composite structure (Saini et al., 2025).

In contrast, the Elovich kinetic model also yields an R^2 value greater than 0.9, suggesting that the active sites in the PSBC/$CoFe_2O_4$/MOF-808 magnetic composite structure are heterogeneous and exhibit varied energies for chemical adsorption (Subramani and Thinakaran, 2017). The parameter α for the adsorption processes of MB and DA were found to be 12.7 and 2.188 mg/g·min, respectively, indicating that MB interacts more strongly with the PSBC/$CoFe_2O_4$/MOF-808 magnetic composite than DA pesticide, thus highlighting the composite's higher adsorption capacity for MB (Kumar et al., 2019).

Furthermore, the linear regression of the intraparticle diffusion model for the adsorption of MB and DA using the PSBC/$CoFe_2O_4$/MOF-808 magnetic composite is depicted in Fig. 7d, with the resulting variables detailed in Table 2. As indicated by the linear regression of the intraparticle diffusion model, the adsorption process of these pollutants involves two distinct stages. The first stage involves film diffusion, where MB and DA molecules move from the aqueous solution to the outer surface of the PSBC/$CoFe_2O_4$/MOF-808 magnetic composite. The second stage relates to intraparticle diffusion, which encompasses the gradual adsorption of these pollutants onto the surface (Meena et al., 2025) and into the pores of the adsorbent structure, resulting in absorption by the internal surface of the adsorbent (Alhamzani et al., 2025). Additionally, it is important to note that none of the lines from the first and second stages intersect the origin in the linear regression of the intraparticle diffusion model ($g_{1,2} \neq 0$), indicating that intraparticle diffusion is not the sole rate-determining step. Other factors, including ion exchange, complexation (Agorku et al., 2025), external mass transfer, intraparticle diffusion, and surface adsorption (Huang et al., 2022), also significantly influence the adsorption process and control its rate.

Table 2
Kinetic constants and variables determined for the removal of MB and DA using the specified adsorbent.

Kinetic model	Pollutants	
	MB	DA
pseudo-first-order		
$q_{e.cal}$	9.742	6.48
k_1	0.102	0.071
R^2	0.876	0.957
Adjusted R^2	0.864	0.953
RMSE	0.606	0.301
pseudo-second-order		
$q_{e.cal}$	10.59	7.286
k_2	0.015	0.013
R^2	0.956	0.981
Adjusted R^2	0.952	0.979
RMSE	0.361	0.201
Elovich		
α	12.7	2.188
β	0.662	0.765
R^2	0.913	0.941
Adjusted R^2	0.904	0.935
RMSE	0.51	0.352
Intra-particle diffusion		
k_{int1}	1.02	0.816
g_1	3.114	0.916
R^2	0.991	0.979
k_{int2}	0.029	0.088
g_2	9.625	5.648
R^2	0.576	0.739

3.4. Isotherm evaluation

To analyze the adsorption isotherms of these pollutants, the Langmuir, Freundlich, and Dubinin-Radushkevich (Dub-Rad) isotherm models were applied, with their nonlinear forms outlined in Equations (9)–(11).

$$\text{Langmuir}: q_e = \frac{q_m K_L C_e}{1 + K_L C_e}, R_L = \frac{1}{1 + K_L C_e} \quad (9)$$

$$\text{Freundlich}: q_e = K_F \; C_e^{1/n} \quad (10)$$

$$\text{Dub} - \text{Rad} :: q_e = q_m \exp(\beta\varepsilon^2), \varepsilon = RT\ln\left(1 + \frac{1}{C_e}\right) \quad (11)$$

Here, q_e (mg/g) represents the adsorption capacities at the equilibrium, K_L (L/mg) is the Langmuir model constant, q_m (mg/g) is the maximum Langmuir adsorption capacity, C_e (mg/L) is the equilibrium concentration of the residual pollutant in the aqueous solution, R_L is the separation factor, n is the adsorption intensity and the heterogeneity within the adsorption system, K_F (L/mg) is the Freundlich model constant and represents the adsorption capacity, β (mol^2/J^2) is the Dub-Rad model constant, and ε (J/mol) is the Polanyi constant.

The nonlinear regression analysis for the Langmuir, Freundlich, and Dubinin-Radushkevich isotherm models applied for MB and DA adsorption using the magnetic composite PSBC/$CoFe_2O_4$/MOF-808 is shown in Fig. 8a and b, with detailed results in Table 3. Among these models, the Freundlich isotherm fits the data best, indicating that the adsorption occurred on a heterogeneous and multilayer surface. The high R^2 and low RMSE values support this. The process showed strong adsorption capacity, particularly for MB dye, with favorable adsorption at high pollutant concentrations (Fang et al., 2024; Kosale et al., 2024; Das and Patel, 2024; Tahir et al., 2024; Varela et al., 2024).

The parameter R_L values for MB and DA decreased as pollutant quantity increased from 5 to 40 mg/L, confirming the effectiveness of the adsorption. The *n* values for MB and DA were 3.666 and 3.269, respectively, while k_L was 4.115 L/mg for MB and 1.25 L/mg for DA, demonstrating the composite's high affinity for these pollutants. The parameter K_F indicated a higher affinity for MB than DA, with values of 20.91 mg/g $(L/mg)^{1/n}$ for MB and 11.18 mg/g $(L/mg)^{1/n}$ for DA. Additionally, the energy parameter E values were below 8 kJ/mol for

Table 3
Isotherm constants and parameters for the removal of MB and DA using the specified adsorbent.

Isotherm models/parameter	Pollutants	
	MB	DA
Langmuir		
q_m (mg/g)	31.44	21.49
K_L (L/mg)	4.115	1.25
R_L	0.006–0.046	0.019–0.137
R^2	0.95	0.909
Adjusted R^2	0.941	0.893
RMSE	2.453	2.046
Freundlich		
n	3.666	3.269
K_F (mg/g $(L/mg)^{1/n}$)	20.91	11.18
R^2	0.971	0.988
Adjusted R^2	0.967	0.986
RMSE	1.847	0.731
Dub–Rad		
E (kJ/mol)	4.322	3.838
q_m (mg/g)	29.05	16.88
β (mol^2/J^2)	2.676 x 10-8	3.394 x 10-8
R^2	0.909	0.769
Adjusted R^2	0.894	0.731
RMSE	3.298	3.256

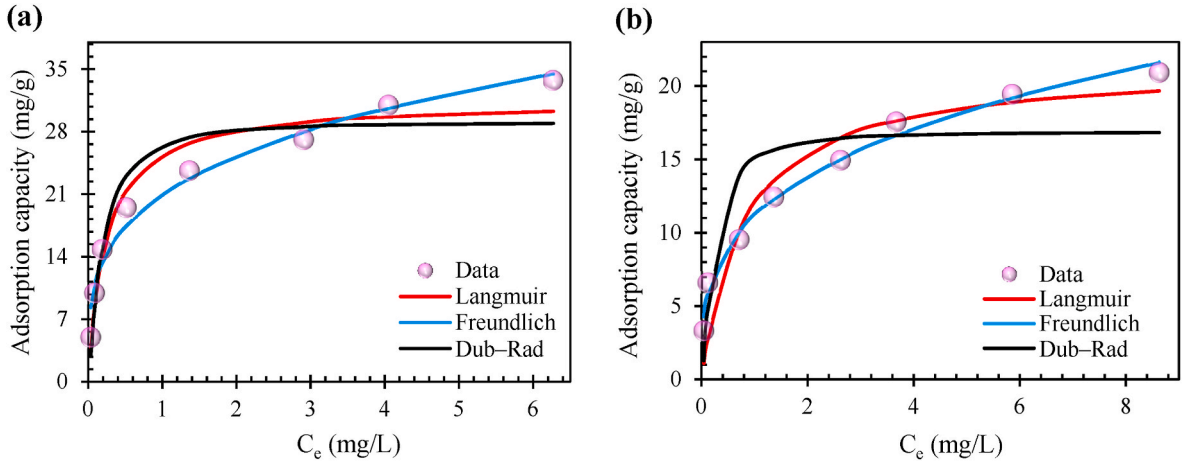

Fig. 8. Nonlinear regression analysis for the isotherm models applied in the removal of **(a)** MB and **(b)** DA using the PSBC/$CoFe_2O_4$/MOF-808.

both pollutants, confirming that physical interactions dominate the adsorption process (Zhang, 2024; Varela et al., 2024).

The maximum monolayer adsorption capacity (q_m) was 31.44 mg/g for MB and 21.49 mg/g for DA, showing that this magnetic composite performs well compared to other adsorbents used for removing similar pollutants (Table 4). This suggests that PSBC/$CoFe_2O_4$/MOF-808 is a promising material for purifying water contaminated with MB and DA toxin.

3.5. Practical applications and reusability assessment

The analysis of the parameters affecting the adsorption process indicated that the magnetic composite PSBC/$CoFe_2O_4$/MOF-808 effectively removes MB and DA from distilled water. Distilled water typically lacks cations and anions, allowing the composite to function without limitations. Given that wastewater and surface water contain various ions and compounds that can compete for active sites on the adsorbent, assessing the composite's performance in different aqueous solutions is essential.

The findings, shown in Fig. 9a, revealed that the removal efficiencies for MB dye were 99.17%, 98.23%, 97.83%, 93.56%, and 87.65% for distilled water, tap water, mineral water, river water, and well water, respectively. The removal efficiencies for DA toxin in these sources were 98.81%, 97.48%, 96.97%, 89.27%, and 82.43%, respectively. The decreased removal efficiencies in river and well water compared to other sources may result from the higher concentrations of organic and inorganic compounds present in these waters, which compete for the adsorptive sites on the adsorbent (Raha and Ahmaruzzaman, 2020).

As time progresses and the active sites on the adsorbent become occupied by target pollutants, the adsorbent's performance and capacity for adsorption diminish. The regeneration of materials are essential for the adsorption process, as they facilitate the removal of adsorbed pollutants and allow for extended usage (Bentouhami et al., 2024). The capability of the PSBC/$CoFe_2O_4$/MOF-808 composite to be regenerated and reused for MB and DA removal was tested across eight cycles, with results displayed in Fig. 9b. The experimental data demonstrated that the composite maintained over 90% efficiency after eight and seven reuse cycles for MB and DA, respectively, indicating its suitability for reuse. However, it is noteworthy that with an increasing number of reuse cycles, the effectiveness of the PSBC/$CoFe_2O_4$/MOF-808 composite in removing MB and DA decreased. This reduction may be due to strong interactions and persistent retention of MB and DA within the adsorbent's micropores (Gavabari et al., 2024), a decrease in available active sites, Partial inactivation of active recruitment sites (Altıntığ et al., 2021) and potential damage to these sites caused by repeated washing and drying (Kumari et al., 2023).

As discussed in the potential mechanism section, Co, Fe, and Zr are crucial for removing MB dye and DA toxicity, acting as effective active sites. To evaluate the stability of the PSBC/$CoFe_2O_4$/MOF-808 magnetic composite after multiple wash and reuse cycles, we analyzed the leaching of Co, Fe, and Zr ions in aqueous solutions using ICP. The results showed concentrations of 0.08, 0.12, and 0.05 mg/L for Co, Fe, and Zr, respectively, indicating minimal leaching and adequate interaction among the composite's components. However, the reduced adsorption efficiency of these pollutants may be linked to ion leaching during washing and reuse.

Additionally, FTIR and VSM analyses were conducted to assess the composite's stability, with results shown in Fig. 10a and b. The FTIR data after two reduction-reuse cycles indicated slight changes in the range and intensity of functional groups, suggesting some groups may have interacted with the MB dye. Despite this, functional groups related to $CoFe_2O_4$ nanoparticles and MOF-808 remained visible (Fig. 10a), confirming their stability and ability to interact with PSBC for repeated use. The VSM analysis revealed that the saturation magnetization of the PSBC/$CoFe_2O_4$/MOF-808 composite decreased from 19.65 emu/g to 18.38 emu/g after two cycles (Fig. 10b), likely due to leaching of Co and Fe ions from the $CoFe_2O_4$ structure.

3.6. Potential mechanism of the adsorption process

The findings from the kinetic, isotherm, thermodynamic studies, and pH effects indicate that several factors such as electrostatic forces, chemical bonds, physical interactions, and the pore structure of the PSBC/$CoFe_2O_4$/MOF-808 magnetic composite—play a crucial role in the adsorption of MB and DA. The active area and pore diameter of this composite were measured at 151.53 m^2/g and 2.518 nm, respectively, suggesting a porous architecture suitable for the infiltration and absorption of the pollutants.

Additionally, investigations into the pH effect revealed that the removal efficiencies of MB and DA reached their highest levels at pH values above and below the pHzpc, which can be attributed to the surface charges of the composite. At pH levels below the pHzpc, the adsorbent carries a positive charge, while it becomes negatively charged at higher pH levels. As the DA toxin converts into anionic species at pH values greater than 2.6 (Moussavi et al., 2013), electrostatic interactions occur between the toxin and the positively charged surface of the adsorbent. Previous research has also identified this as an effective mechanism for removing both DA and MB (Baharum et al., 2020; Cao et al., 2024). In contrast, the positively charged MB interacts with the

Table 4
Comparison of the adsorption capacities of different adsorbents for MB and DA elimination, including the PSBC and PSBC/$CoFe_2O_4$/MOF-808.

Adsorbent	q_m MB (mg/g)	q_m DA (mg/g)	Reference
NC-MgO	–	20	Armaghan and Amini (2017)
CM-MgO	–	12	Armaghan and Amini (2017)
Fe_3O_4@SiO_2 magnetic	–	10.90	Shamsizadeh et al. (2020)
MOF UiO-66	–	4.4	Ashouri et al. (2021)
MIL-101(Cr)	–	19.58	Shadmehr et al. (2019)
Acid activated bentonite	–	5.563	Ouznadji et al. (2016)
pre-treated coffee waste	–	18.52	Yeddou Mezenner et al. (2017)
Phosphoric acid coconut shell biochar	–	10.33	Baharum et al. (2020)
kaolinite modified with benzalkonium chloride	–	19.23	Tilaki et al. (2020)
Fe_3O_4·CuO	–	0.0254	Yeganeh-Faal and Kadkhodaei (2022)
MIP-202/CA composite beads	–	17.776	Diab et al. (2021)
acid treated zeolite	–	15.10	Esfandian et al. (2016)
Cu_2O nanoparticles	–	61.73	Esfandian et al. (2016)
clay/GO/Fe_3O_4	–	7.384	Sohrabi et al. (2021)
StP-*g*-PIMDZ 3	5.37	–	Haq et al. (2023)
Fe_3O_4/AC/CD/Alg polymer dry powder beads	10.63	–	Yadav et al. (2020)
Fe_3O_4/AC/CD/Alg polymer gel beads	2.079	–	Yadav et al. (2020)
magnetized corn cobs	13.23	–	Allou et al. (2023)
MIL-101(Cr)	8.9	–	Chang et al. (2018)
TiO_2-MIL-101(Cr)	20.7	–	Chang et al. (2018)
MIL-101(Cr^{3+}) (Samples: A_0 – B_3)	2.47–26.46	–	Shen et al. (2015)
MIL101-Cr/PANI/Ag	43.29	–	Karami et al. (2022)
Fe_3O_4/Cu_3(BTC)$_2$	25	–	Zhao et al. (2015)
UiO-66	24.5	–	Yang (2017)
Cu-BTC samples	11.10–15.28	–	Lin et al. (2014)
$MnFe_2O_4$@Zn-Al LDHs@Cel@AGB	34.19	–	Mahmoud et al. (2021)
PSBC/$CoFe_2O_4$/MOF-808	31.44	21.49	Present study

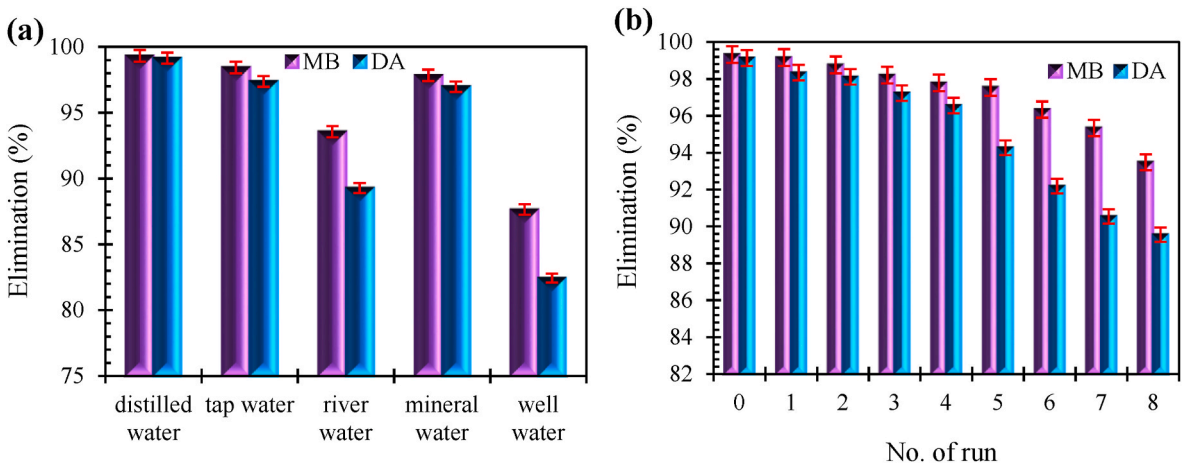

Fig. 9. **(a)** The effect of different water sources on the ability of the PSBC/$CoFe_2O_4$/MOF-808 to remove MB and DA, **(b)** The reusability of the PSBC/$CoFe_2O_4$/MOF-808 in removing MB and DA (pH levels for removing MB and DA are 9 and 6, respectively; adsorbent doses for removing MB and DA are 1 and 1.5 g/L, respectively; temperature 55 °C; contact times for removing MB and DA are 60 and 80 min, respectively; initial concentrations of MB and DA are 5 mg/L).

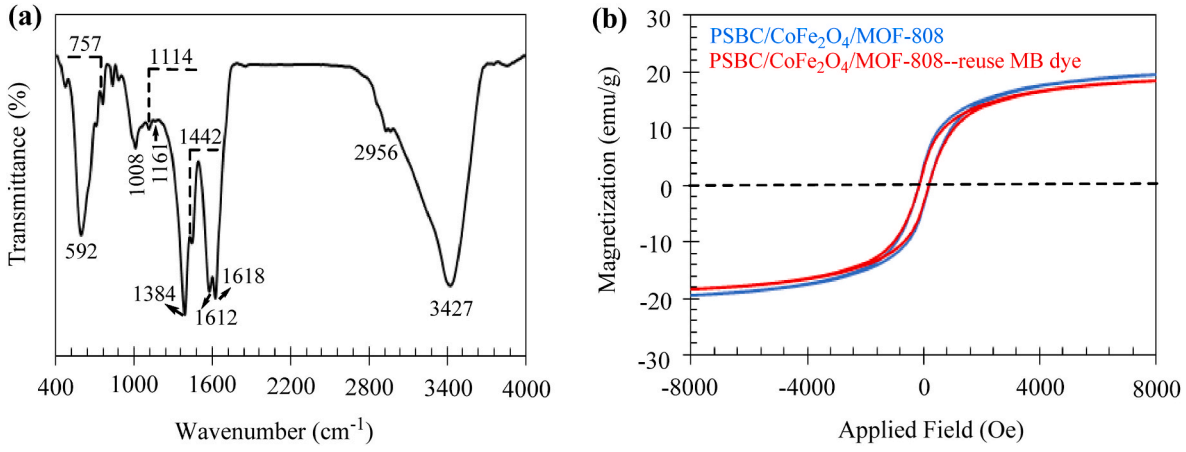

Fig. 10. **(a)** FTIR spectrum and **(b)** VSM analysis of the PSBC/$CoFe_2O_4$/MOF-808 after two reuse cycles of MB.

negatively charged surface of the adsorbent at pH values exceeding the pHzpc.

In addition to electrostatic attraction, interactions between functional groups and those in the pollutants can serve as important mechanisms. FTIR analysis revealed the presence C=O, C=C, -OH, Zr-O, Fe-O/Co-O, and C-H within the PSBC/$CoFe_2O_4$/MOF-808 composite structure. The oxygen and hydrogen functional groups can form hydrogen bonds with the constituents of the DA toxin and MB dye, thereby facilitating their removal from aqueous solutions (Alrefaee et al., 2023). Notably, hydrogen bonding may occur between the nitrogen and sulfur in the MB and DA structures and the -OH functional groups in the composite (Yang et al., 2024).

Additionally, the -OH functional groups in the composite can form Yoshida hydrogen bonds with the aromatic rings in the pollutants, promoting their adsorption and interaction with the magnetic adsorbent (Wang et al., 2024e). Another relevant interaction is the π-π interaction; FTIR results indicate the presence of C=C/C=O in PSBC/$CoFe_2O_4$/-MOF-808, likely originating from either the PSBC structure or the MOF-808 ligand. Consequently, these functional groups can establish π-π interactions with the aromatic rings of the MB and DA, leading to their removal (Azim et al., 2024; Wang et al., 2024f).

Furthermore, FTIR test confirmed the existence of oxygen-containing groups (C=O), with oxygen in the composite acting as an electron donor, which can promote n-π interactions with the aromatic rings of the pollutants, thereby enhancing adsorption (Grich et al., 2024). Additionally, cation-π interactions play a significant role in the removal of MB and DA. Based on FTIR and XRD results, the presence of Co, Fe, and Zr within the magnetic composite can facilitate cation-π interactions with the unsaturated bonds of the aromatic rings in the pollutants, aiding in their removal from aqueous solutions (Zhang et al., 2019). Additionally, XRD, EDX, and FTIR analyses have validated the presence of metal oxides Fe-O, Co-O, and Zr-O in the PSBC/$CoFe_2O_4$/MOF-808 composite, which contain -OH functional groups on their surfaces. These groups can play a vital role in complexation, thereby enhancing the removal of pollutants through complex formation (Ma et al., 2024; Li et al., 2022). To examine the influence of functional groups and pores in the PSBC/$CoFe_2O_4$/-MOF-808 magnetic composite on the adsorption of MB dye and DA toxicity, we conducted SEM and EDX analyses (Fig. 11a and b). The findings reveal that after the adsorption process, nitrogen (N) and sulfur (S) elements, which are part of the MB and DA, appeared in the composite structure. The presence of N and S indicates that the composite effectively adsorbs these pollutants, which are likely retained in the pores and interact with the functional groups of the composite.

4. Conclusions

This study aimed to synthesize PSBC modified with $CoFe_2O_4$ and MOF-808 magnetic nanoparticles (PSBC/$CoFe_2O_4$/MOF-808) and evaluate its effectiveness in removing MB dye and DA toxin from water. The composite was successfully prepared, exhibiting a saturation

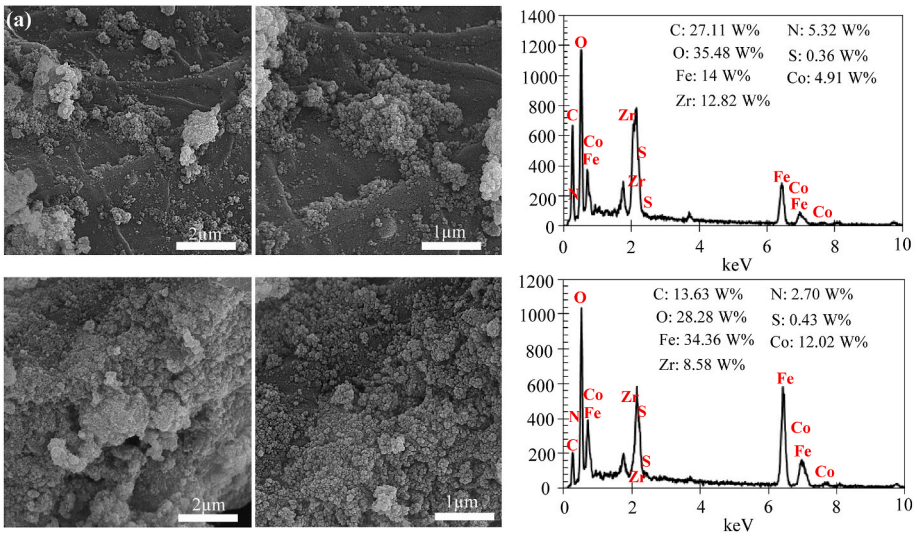

Fig. 11. SEM and EDX images of PSBC/$CoFe_2O_4$/MOF-808 after the adsorption of **(a)** MB and **(b)** DA.

magnetization of 19.65 emu/g and a specific surface area of 151.53 m^2/g. Results showed that pollutant removal improved with increased temperature, contact time, adsorbent dosage, and pH, while higher initial concentrations hindered efficiency. Under optimal conditions, maximum removal efficiencies reached 99.32% for MB and 99.14% for DA. The adsorption process was spontaneous, as indicated by negative ΔG values, and endothermic, as revealed by ΔH and ΔS parameters. Adsorption followed the pseudo-second-order kinetic model, highlighting the role of chemical interactions, and equilibrium data aligned closely with the Freundlich isotherm, pointing to the significance of heterogeneous surface interactions. Reusability tests confirmed the composite's strong regeneration capacity, demonstrating effective performance over multiple cycles.

Future investigations could explore the long-term stability and performance of the PSBC/$CoFe_2O_4$/MOF-808 composite under varying environmental conditions and multiple reuse cycles. Additionally, further research may focus on optimizing the composite's adsorption efficiency for other pollutants and investigating its potential for large-scale applications in diverse water sources.

CRediT authorship contribution statement

Sattam Fahad Almojil: Writing – original draft, Supervision, Methodology, Investigation, Funding acquisition, Conceptualization. **Abdulaziz Ibrahim Almohana:** Writing – review & editing, Writing – original draft, Software, Methodology, Formal analysis.

Declaration of competing interest

The authors declare that they have no known competing financial interests or personal relationships that could have appeared to influence the work reported in this paper.

Acknowledgement

This research was supported by the Researchers Supporting Project, number (RSP2025R303), at King Saud University, Riyadh, Saudi Arabia.

Data availability

Data will be made available on request.

References

Abdel-Fattah, E., Alharthi, A.I., Alotaibi, M.A., 2024. Synergetic effects of Al addition on the performance of $CoFe_2O_4$ catalyst for hydrogen production and filamentous carbon formation from direct cracking of methane. J. Alloys Compd. 997, 174982.

Adhikari, S., Moon, E., Paz-Ferreiro, J., Timms, W., 2024. Comparative analysis of biochar carbon stability methods and implications for carbon credits. Sci. Total Environ. 914, 169607.

Adibzadeh, A., Khodabakhshi, M.R., Maleki, A., 2024. Preparation of novel and recyclable chitosan-alumina nanocomposite as superabsorbent to remove diazinon and tetracycline contaminants from aqueous solution. Helyon 10 (1).

E.S. Agorku, A. Kangmennaa, B.Y. Danu, F.K. Ampong, R.B. Voegborlo, Core-shell V2O5-Gum ghatti grafted poly (acrylamide-co-methacrylic acid) adsorbent for the removal of methylene blue dye in water: kinetic, equilibrium and thermodynamic studies, Sustainability 5 (2025) 100069.

Ahmed, S., Ferdous, Z., 2024. Prospective application of eco-friendly banana peel reduced graphene oxide (BRGO) for aqueous Cr (VI) and acid dye adsorption: a waste utilization approach. Bioresour. Technol. Rep. 27, 101936.

Ajami, A., Sheibani, S., Ataie, A., 2024. S-scheme $CoFe_2O_4$/g-C_3N_4 nanocomposite with high photocatalytic activity and antibacterial capability under visible light irradiation. J. Mater. Res. Technol. 30, 2168–2185.

Al-Sareji, O.J., Al-Samarrai, S.Y., Grmasha, R.A., Meiczinger, M., Al-Juboori, R.A., Jakab, M., Somogyi, V., Miskolczi, N., Hashim, K.S., 2024. A novel and sustainable composite of L@ PSAC for superior removal of pharmaceuticals from different water matrices: production, characterization, and application. Environ. Res. 251, 118565.

K. Alhamzani, H. El-Hamshary, S. Alterary, B.M. Thamer, M.M. Abdulhameed, M. El-Newehy, Synthesis of pyridine-quaternized chloroethyl vinyl ether copolymers as adsorbents for Eosin dye removal from wastewater, J. Mol. Struct. 1319 (2025) 139468.

Alharthi, A.I., Alotaibi, M.A., Abdel-Fattah, E., Awadallah, A.E., 2024. Understanding the impact of support materials on $CoFe_2O_4$ catalyst performance for hydrogen fuel and nanocarbon production via methane decomposition. Ceram. Int. 50 (20), 38029–38039.

Allou, N.g.B., Tigori, M.A., Koffi, A.A., Halidou, M., Eroi, N.g.S., Atheba, P., Trokourey, A., 2023. Methylene blue magnetic adsorption separation process from aqueous solution using corn cob. Scientific African 21, e01828. https://doi.org/10.1016/j.sciaf.2023.e01828.

Alonso-Gómez, L., Celis-Carmona, D., Rodríguez-Sánchez, Y., Castro-Ladino, J., Solarte-Toro, J., 2024. Biochar production from cassava waste biomass: a techno-economic development approach in the Colombian context. Bioresour. Technol. Rep., 101872

Alrefaee, S.H., Aljohani, M., Alkhamis, K., Shaaban, F., El-Desouky, M.G., El-Bindary, A. A., El-Bindary, M.A., 2023. Adsorption and effective removal of organophosphorus pesticides from aqueous solution via novel metal-organic framework: adsorption isotherms, kinetics, and optimization via Box-Behnken design. J. Mol. Liq. 384, 122206.

Altıntıg, E., Altundag, H., Tuzen, M., Sarı, A., 2017. Effective removal of methylene blue from aqueous solutions using magnetic loaded activated carbon as novel adsorbent. Chem. Eng. Res. Des. 122, 151–163. https://doi.org/10.1016/j.cherd.2017.03.035.

Altıntıg, E., Yenigun, M., Sarı, A., Altundag, H., Tuzen, M., Saleh, T.A., 2021. Facile synthesis of zinc oxide nanoparticles loaded activated carbon as an eco-friendly adsorbent for ultra-removal of malachite green from water. Environmental Technology & Innovation 21, 101305. https://doi.org/10.1016/j.eti.2020.101305.

Amedi, H.R., Aghajani, M., 2017. Aminosilane-functionalized ZIF-8/PEBA mixed matrix membrane for gas separation application. Microporous Mesoporous Mater. 247, 124–135.

Amusat, S.O., Kebede, T.G., Nxumalo, E.N., Dube, S., Nindi, M.M., 2022. Incorporating pristine biochar into metal-organic frameworks: facile green synthesis,

characterization, and wastewater remediation. Bioresour. Technol. Rep. 19, 101160. https://doi.org/10.1016/j.biteb.2022.101160.
Armaghan, M., Amini, M.M., 2017. Adsorption of diazinon and fenitrothion on nanocrystalline magnesium oxides. Arab. J. Chem. 10 (1), 91–99. https://doi.org/10.1016/j.arabjc.2014.01.002.
Ashouri, V., Adib, K., Nasrabadi, M.R., Ghalkhani, M., 2021. Preparation of the extruded UiO-66-based Metal-Organic Framework for the diazinon removal from the real samples. J. Mol. Struct. 1240, 130607. https://doi.org/10.1016/j.molstruc.2021.130607.
Azim, E.A., Samy, M., Hanafy, M., Mahanna, H., 2024. Novel mint-stalks derived biochar for the adsorption of methylene blue dye: effect of operating parameters, adsorption mechanism, kinetics, isotherms, and thermodynamics. J. Environ. Manag. 357, 120738.
Badamasi, H., Sanni, S.O., Ore, O.T., Bayode, A.A., Koko, D.T., Akeremale, O.K., Emmanuel, S.S., 2024. Eggshell waste materials-supported metal oxide nanocomposites for the efficient photocatalytic degradation of dyes in water and wastewater: a review. Bioresour. Technol. Rep., 101865
Baharum, N.A., Nasir, H.M., Ishak, M.Y., Isa, N.M., Hassan, M.A., Aris, A.Z., 2020. Highly efficient removal of diazinon pesticide from aqueous solutions by using coconut shell-modified biochar. Arab. J. Chem. 13 (7), 6106–6121.
X. Bao, J. Li, J. Shen, X. Chen, C. Zhang, H. Cui, Comprehensive multivariate joint distribution model for marine soft soil based on the vine copula, Comput. Geotech. 177 (2025) 106814.
Bazarin, G., Módenes, A.N., Espinoza-Quiñones, F.R., Borba, C.E., Trigueros, D.E.G., Dall'Oglio, I.C., 2024. High removal performance of reactive blue 5G dye from industrial dyeing wastewater using biochar in a fixed-bed adsorption system: Approaches and insights based on modeling, isotherms, and thermodynamics study. J. Environ. Chem. Eng. 12 (1), 111761. https://doi.org/10.1016/j.jece.2023.111761.
Behera, A.K., Shadangi, K.P., Sarangi, P.K., 2024. Efficient removal of Rhodamine B dye using biochar as an adsorbent: study the performance, kinetics, thermodynamics, adsorption isotherms and its reusability. Chemosphere 354, 141702.
Bellaj, M., Aziz, K., El Achaby, M., El Haddad, M., Gebrati, L., Kurniawan, T.A., Chen, Z., Yap, P.-S., Aziz, F., 2024. Cationic and anionic dyes adsorption from wastewater by clay-chitosan composite: an integrated experimental and modeling study. Chem. Eng. Sci. 285, 119615.
Bentouhami, E., Zaghouane-Boudiaf, H., Touahria, Y.I., Bellil, G., Boublia, A., Daas, N., Dintzer, T., Chafai, N., Albrahim, M., Elboughdiri, N., 2024. Efficient wastewater decontamination using magnetic bentonite-alginate beads: a comprehensive study of adsorption dynamics, regeneration, and molecular interactions. J. Environ. Chem. Eng. 12 (3), 113000.
Bhat, S.A., Tantray, A.M., Ahsan, J.U., Ikram, M., 2024. Exploring the supercapacitive potential of Sm3+ doped CoFe2O4 nanoparticles: enhanced magnetic and dielectric properties. Ceram. Int.
Cai, H., Zhang, L., Wei, J., Hou, Y., Wei, Y., Zhou, S., Jia, Z., Su, X., 2024. Ultra-efficient and selective adsorption of cationic dyes by Ti-doped SiO_2 functionalized hydrophilic Fe_3O_4 nanoparticles with superior structural stability. Journal of Water Process Engineering 57, 104729.
Cao, Y., Yang, L., Liu, F., Yu, Q., 2024. Adsorption experiments and mechanisms of methylene blue on activated carbon from garden waste via deep eutectic solvents coupling KOH activation. Biomass Bioenergy 182, 107074.
Chaima, H., Eddine, B.C., Faouzia, B., Rana, H., Salah, B.A., Gil, A., Imene, B.-A., Ferhat, D., Riadh, B., Mokhtar, B., 2024. Adsorptive removal of cationic dye from aqueous solutions using activated carbon prepared from *Crataegus monogyna*/sodium alginate/polyaniline composite beads: experimental study and molecular dynamic simulation. J. Mol. Liq. 408, 125372.
Chang, N., Zhang, H., Shi, M.-S., Li, J., Yin, C.-J., Wang, H.-T., Wang, L., 2018. Regulation of the adsorption affinity of metal-organic framework MIL-101 via a TiO_2 coating strategy for high capacity adsorption and efficient photocatalysis. Microporous Mesoporous Mater. 266, 47–55. https://doi.org/10.1016/j.micromeso.2018.02.051.
Chang, S., Zhang, Q., Lu, Y., Wu, S., Wang, W., 2020. High-efficiency and selective adsorption of organic pollutants by magnetic $CoFe_2O_4$/graphene oxide adsorbents: experimental and molecular dynamics simulation study. Separation and Purification Technology 238, 116400.
Chen, B., Cao, Y., Zhao, H., Long, F., Feng, X., Li, J., Pan, X., 2020. A novel Fe^{3+}-stabilized magnetic polydopamine composite for enhanced selective adsorption and separation of Methylene blue from complex wastewater. J. Hazard Mater. 392, 122263.
Chen, L., Zhu, Y., Cui, Y., Dai, R., Shan, Z., Chen, H., 2021. Fabrication of starch-based high-performance adsorptive hydrogels using a novel effective pretreatment and adsorption for cationic methylene blue dye: behavior and mechanism. Chem. Eng. J. 405, 126953.
Chen, L., Zhai, S., Yang, L., Chen, K., Li, Z., Yu, T., Xie, H., Zhu, H., 2024. Self-enhancement of phosphorus recovery from anaerobic fermented sludge with MOF-808 synthesized with an improved green method. Chem. Eng. J. 479, 147880.
Damahe, D., Mayilswamy, N., Kandasubramanian, B., 2024. Biochar/metal nanoparticles-based composites for Dye remediation: a review. Hybrid Advances 6, 100254. https://doi.org/10.1016/j.hybadv.2024.100254.
Damiri, F., Dobaradaran, S., Hashemi, S., Foroutan, R., Vosoughi, M., Sahebi, S., Ramavandi, B., Camilla Boffito, D., 2020. Waste sludge from shipping docks as a catalyst to remove amoxicillin in water with hydrogen peroxide and ultrasound. Ultrason. Sonochem. 68, 105187. https://doi.org/10.1016/j.ultsonch.2020.105187.
Daneshvar, S., Mosaddeghi, M.R., Afyuni, M., 2024. Effect of biochar and hydrochar of pistachio residues on physical quality indicators of a sandy loam soil. Geoderma Regional 36, e00740.
Das, T., Patel, D.K., 2024. Efficient removal of cationic dyes using lemon peel-chitosan hydrogel composite: RSM-CCD optimization and adsorption studies. Int. J. Biol. Macromol. 275, 133561.
Dashtipour, B., Dehghanpour, S., Sharbatdaran, M., 2024. Enhanced acidity of MOF-808 by defect-engineered and supported-sulfuric acid in ketalization of glycerol. Polyhedron 247, 116733.
de Benedicto, D.F.C., Ferreira, G.M.D., Thomasi, S.S., 2024. β-cyclodextrin-functionalized coffee husk biochar for surfactant adsorption. Colloids Surf. A Physicochem. Eng. Asp. 701, 134921.
Değermenci, G.D., Değermenci, N., Ayvaoğlu, V., Durmaz, E., Çakır, D., Akan, E., 2019. Adsorption of reactive dyes on lignocellulosic waste; characterization, equilibrium, kinetic and thermodynamic studies. J. Clean. Prod. 225, 1220–1229.
Del Pozo, C., Rego, F., Puy, N., Bartrolí, J., Fàbregas, E., Yang, Y., Bridgwater, A.V., 2022. The effect of reactor scale on biochars and pyrolysis liquids from slow pyrolysis of coffee silverskin, grape pomace and olive mill waste, in auger reactors. Waste Management 148, 106–116.
Diab, K.E., Salama, E., Hassan, H.S., El-moneim, A.A., Elkady, M.F., 2021. Bio-Zirconium metal–organic framework regenerable bio-beads for the effective removal of organophosphates from polluted water. Polymers 13 (22), 3869.
Dong, N., Zhong, M., Fei, P., Lei, Z., Su, B., 2016. Magnetic and electrochemical properties of PANI-$CoFe_2O_4$ nanocomposites synthesized via a novel one-step solvothermal method. J. Alloys Compd. 660, 382–386.
Duwiejuah, A.B., Adjei, E.F., Alhassan, E.H., 2024. Adsorption of toxic metals from greywater using coconut husk biochar and spent green tea. Heliyon 10 (18), e38189. https://doi.org/10.1016/j.heliyon.2024.e38189.
Ehsani, A., Aghdasinia, H., Farshchi, M.E., Rostamnia, S., Khataee, A., 2023. Synthesis of sodium alginate/carboxy-methyl cellulose/Cu-based metal-organic framework composite for adsorption of tetracycline from aqueous solution: isotherm, kinetic and thermodynamic approach. Surface. Interfac. 36, 102506. https://doi.org/10.1016/j.surfin.2022.102506.
El-Desouky, M.G., Alayyafi, A.A., Al-Hazmi, G.A., El-Bindary, A.A., 2024. Effect of metal organic framework alginate aerogel composite sponge on adsorption of tartrazine from aqueous solutions: adsorption models, thermodynamics and optimization via Box-Behnken design. J. Mol. Liq. 399, 124392.
Esfandian, H., Samadi-Maybodi, A., Parvini, M., Khoshandam, B., 2016. Development of a novel method for the removal of diazinon pesticide from aqueous solution and modeling by artificial neural networks (ANN). J. Ind. Eng. Chem. 35, 295–308. https://doi.org/10.1016/j.jiec.2016.01.011.
Fan, J., Pan, Y., Wang, H., Song, F., 2024a. Efficient reverse osmosis-based desalination using functionalized graphene oxide nanopores. Appl. Surf. Sci. 674, 160937.
Fan, J., Zhang, X., He, N., Song, F., Zhang, X., 2024b. Physical absorption and thermodynamic modeling of CO_2 in new deep eutectic solvents. J. Mol. Liq. 402, 124752.
Fang, W., Zhou, Y., Cheng, M., Yang, J., Huang, Q., Huang, Z., Cui, Y., Zhang, L., Wang, Y., Cen, Q., 2024. Effective adsorption performance and mechanism of methylene blue from dye wastewater by humic acid sucrose-modified red mud. Process Saf. Environ. Protect. 191, 1168–1180.
Farmany, A., Mortazavi, S.S., Mahdavi, H., 2016. Ultrasond-assisted synthesis of Fe_3O_4/SiO_2 core/shell with enhanced adsorption capacity for diazinon removal. J. Magn. Magn Mater. 416, 75–80.
Fu, Q., Liu, D., Niu, W., Zhang, S., Chen, R., Wang, Y., Zhao, P., Jiang, H., Zhao, Y., Yang, L., 2022. Defect-engineered MOF-808 with highly exposed Zr sites as highly efficient catalysts for catalytic transfer hydrogenation of furfural. Fuel 327, 125085.
Gao, F., Xu, Z., Dai, Y., 2021. Removal of tetracycline from wastewater using magnetic biochar: a comparative study of performance based on the preparation method. Environmental Technology & Innovation 24, 101916.
Gavabari, S.E., Goudarzi, A., Shahrousvand, M., Asfaram, A., 2024. Preparation of novel polyurethane/activated carbon/cellulose nano-whisker nanocomposite film as an efficient adsorbent for the removal of methylene blue and basic violet 16 dyes from wastewater. Separation and Purification Technology 330, 125285.
R. Ghasemzadeh, K. Akhbari, Degradation of acid blue 41 with carbon quantum dots@MOF-808 nanocomposite as a biocompatible photocatalyst under visible light, J. Photochem. Photobiol. Chem. 458 (2025) 115984.
Gong, H., Sardans, J., Huang, H., Yan, Z., Wang, Z., Peñuelas, J., 2024. Global patterns and controlling factors of tree bark C: N: P stoichiometry in forest ecosystems consistent with biogeochemical niche hypothesis. New Phytol.
Grich, A., Bouzid, T., Naboulsi, A., Regti, A., Tahiri, A.A., El Himri, M., El Haddad, M., 2024. Preparation of low-cost activated carbon from Doum fiber (*Chamaerops humilis*) for the removal of methylene blue: optimization process by DOE/FFD design, characterization, and mechanism. J. Mol. Struct. 1295, 136534.
Hameed, M.M.A., Al-Aizari, F.A., Thamer, B.M., 2024. Synthesis of a novel clay/polyacrylic acid-tannic acid hydrogel composite for efficient removal of crystal violet dye with low swelling and high adsorption performance. Colloids Surf. A Physicochem. Eng. Asp. 684, 133130.
Haq, F., Kiran, M., Chinnam, S., Farid, A., Khan, R.U., Ullah, G., Aljuwayid, A.M., Habila, M.A., Mubashir, M., 2023. Synthesis of bioinspired sorbent and their exploitation for methylene blue remediation. Chemosphere 321, 138000. https://doi.org/10.1016/j.chemosphere.2023.138000.
Hashemkhani, M., Rezvani Ghalhari, M., Bashardoust, P., Hosseini, S.S., Mesdaghinia, A., Mahvi, A.H., 2022. Fluoride removal from aqueous solution via environmentally friendly adsorbent derived from seashell. Sci. Rep. 12 (1), 9655.
Hassaan, M.A., Elkatory, M.R., El-Nemr, M.A., Ragab, S., Yi, X., Huang, M., El Nemr, A., 2024. Synthesis, characterization, optimization and application of Pisum sativum peels S and N-doping biochars in the production of biogas from Ulva lactuca. Renew. Energy 221, 119747.

Hassan, A.F., Elhadidy, H., Abdel-Mohsen, A., 2017. Adsorption and photocatalytic detoxification of diazinon using iron and nanotitania modified activated carbons. J. Taiwan Inst. Chem. Eng. 75, 299–306.
He, W., Wu, J., Liu, J., Li, J., 2024. Single-Atom Nanozymes for catalytic Therapy: Recent Advances and challenges. Adv. Funct. Mater. 34 (16), 2312116.
Heydari, F., Afghahi, S.S., Valmoozi, A.E., 2024. A study on the structural, magnetic, and electromagnetic wave absorption properties of $CoFe_2O_4$@ MWCNT nanocomposites. J. Magn. Magn Mater., 172273
Hu, H., Zhang, J., Wang, T., Wang, P., 2022. Adsorption of toxic metal ion in agricultural wastewater by torrefaction biochar from bamboo shoot shell. J. Clean. Prod. 338, 130558. https://doi.org/10.1016/j.jclepro.2022.130558.
Huang, Q., Zhao, L., Zhu, G., Chen, D., Ma, X., Yang, X., Wang, S., 2022. Outstanding performance of thiophene-based metal-organic frameworks for fluoride capture from wastewater. Separation and Purification Technology 298, 121567.
Huang, B., Kang, F., Li, X., Zhu, S., 2024a. Underwater dam crack image generation based on unsupervised image-to-image translation. Autom. ConStruct. 163, 105430.
Huang, B., Wang, R., Hu, W., Xu, H., Chen, Q., Liu, T., Fan, Y., Kong, Y., 2024b. Preparation and performance of MOF-808 (Zr-MOF) for the efficient adsorption of phenoxyacetic acid pesticides. J. Ind. Eng. Chem.
Huerta-Flores, A.M., Torre, F., Taeño, M., Barreno, R.C., Del Barrio, E.P., Doppiu, S., 2024. Influence of physicochemical properties on the thermochemical water splitting performance and H_2 production of $CoFe_2O_4$. Int. J. Hydrogen Energy 71, 1293–1302.
Inamdar, A.K., Rajenimbalkar, R.S., Hulsure, N.R., Kadam, A.S., Shinde, B.H., Patole, S. P., Shelke, S.B., Inamdar, S.N., 2023. A review on environmental applications of metal oxide nanoparticles through waste water treatment. Mater. Today: Proc. https://doi.org/10.1016/j.matpr.2023.05.527.
Jalayeri, H., Pepe, F., 2019. Novel and high-performance biochar derived from pistachio green hull biomass: production, characterization, and application to Cu (II) removal from aqueous solutions. Ecotoxicology and environmental safety 168, 64–71.
Kapur, M.A., Devi, M.K., Janani, R., Prasanna, J., Arumugam, N., Djearamane, S., Wong, L.S., Kayarohanam, S., 2024. Simple biotic; spinel $CoFe_2O_4$ nanosphere for textile pollutant removal by photoresponsivity process and Anti-Microbial analysis. J. King Saud Univ. Sci. 36 (9), 103369.
Karami, K., Beram, S.M., Bayat, P., Siadatnasab, F., Ramezanpour, A., 2022. A novel nanohybrid based on metal–organic framework MIL101−Cr/PANI/Ag for the adsorption of cationic methylene blue dye from aqueous solution. J. Mol. Struct. 1247, 131352. https://doi.org/10.1016/j.molstruc.2021.131352.
Kazemi, A., Pordsari, M.A., Tamtaji, M., Afshari, M.H., Keshavarz, S., Zeinali, F., Baesmat, H., Zahiri, S., Manteghi, F., Ghaemi, A., 2024. Unveiling the power of defect engineering in MOF-808 to enhance efficient carbon dioxide adsorption and separation by harnessing the potential of DFT analysis. Chem. Eng. J. 494, 153049.
Khaledian, S., Noroozi-Aghideh, A., Kahrizi, D., Moradi, S., Abdoli, M., Ghasemalian, A. H., Heidari, M.F., 2021. Rapid detection of diazinon as an organophosphorus poison in real samples using fluorescence carbon dots. Inorg. Chem. Commun. 130, 108676.
Khanahmadi, S., Masoudpanah, S., 2024. Preparation and microwave absorption properties of $CoFe_2O_4$/$NiCo_2O_4$ composite powders. Ceram. Int. 50 (6), 9779–9788.
Kopp Alves, A., Hauschild, T., Basegio, T.M., Amorim Berutti, F., 2024. Influence of lignin and cellulose from termite-processed biomass on biochar production and evaluation of chromium VI adsorption. Sci. Rep. 14 (1), 14937.
Kosale, D., Singh, V.K., Thakur, C., 2024. Comparative adsorption of cationic and anionic dye by using non-activated Black Plum seed biochar for aquatic phase: isotherm, kinetic and thermodynamic studies. Ind. Crop. Prod. 215, 118609.
Kumar, R., Sharma, R.K., Singh, A.P., 2019. Sorption of Ni (II), Pb (II) and Cu (II) ions from aqueous solutions by cellulose grafted with poly (HEMA-co-AAc): kinetic, isotherm and thermodynamic study. J. Environ. Chem. Eng. 7 (3), 103088.
Kumari, N., Behera, M., Singh, R., 2023. Facile synthesis of biopolymer decorated magnetic coreshells for enhanced removal of xenobiotic azo dyes through experimental modelling. Food Chem. Toxicol. 171, 113518. https://doi.org/10.1016/j.fct.2022.113518.
Lakshmigandhan, T., Nithiyanantham, S., Mahalakshmi, S., Kogulakrishnan, K., Mohan, R., Gunasekaran, B., Palaniappan, L., 2024. Structural, electrical and magnetic studies on $CoFe_2O_4$ nanoparticles with polyvinylalcohol (PVA) via Sol-Gel approach. Mater. Sci. Eng., B 307, 117494.
Lee JeChan, L.J., Yang Xiao, Y.X., Cho SeongHeon, C.S., Kim JaeKon, K.J., Lee SangSoo, L.S., Tsang, D., Ok YongSik, O.Y., Kwon, E., 2017. Pyrolysis process of agricultural waste using CO2 for waste management, energy recovery, and biochar fabrication.
Li, D., Hua, T., Yuan, J., Xu, F., 2021. Methylene blue adsorption from an aqueous solution by a magnetic graphene oxide/humic acid composite. Colloids Surf. A Physicochem. Eng. Asp. 627, 127171.
Li, B., Zhang, Y., Xu, J., Fan, S., Xu, H., 2022. Facile preparation of magnetic porous biochars from tea waste for the removal of tetracycline from aqueous solutions: effect of pyrolysis temperature. Chemosphere 291, 132713.
Li, B., Lin, X., Zhao, Y., 2024. Facile preparation and application of magnetic chitosan/fly ash composite as a hybrid biosorbent for the effective removal of direct dyes. J. Mol. Liq. 397, 124148.
Lin, S., Song, Z., Che, G., Ren, A., Li, P., Liu, C., Zhang, J., 2014. Adsorption behavior of metal–organic frameworks for methylene blue from aqueous solution. Microporous Mesoporous Mater. 193, 27–34. https://doi.org/10.1016/j.micromeso.2014.03.004.
Liu, W., Huang, F., Liao, Y., Zhang, J., Ren, G., Zhuang, Z., Zhen, J., Lin, Z., Wang, C., 2008. Treatment of CrVI-containing Mg $(OH)_2$ nanowaste. Angew. Chem. 120 (30), 5701–5704.
Liu, W., Zheng, J., Ou, X., Liu, X., Song, Y., Tian, C., Rong, W., Shi, Z., Dang, Z., Lin, Z., 2018. Effective extraction of Cr (VI) from hazardous gypsum sludge via controlling the phase transformation and chromium species. Environmental science & technology 52 (22), 13336–13342.
Liu, J., Liu, T., Su, C., Zhou, S., 2023. Operation analysis and its performance optimizations of the spray dispersion desulfurization tower for the industrial coal-fired boiler. Case Stud. Therm. Eng. 49, 103210.
P. Liu, J. Lyu, P. Bai, Synthesis of mixed matrix membrane utilizing robust defective MOF for size-selective adsorption of dyes, Separation and Purification Technology 354 (2025) 128672.
Ma, L., Liu, W., Liu, B., Tang, Y., 2024. Removal of methylene blue by acrylic polymer adsorbents loaded with magnetic iron manganese oxides: synthesis, characterization, and adsorption mechanisms. Chemosphere 346, 140588.
Mahmoud, M.E., El-Bahy, S.M., Elweshahy, S.M.T., 2021. Decorated Mn-ferrite nanoparticle@Zn–Al layered double hydroxide@Cellulose@ activated biochar nanocomposite for efficient remediation of methylene blue and mercury (II). Bioresour. Technol. 342, 126029. https://doi.org/10.1016/j.biortech.2021.126029.
Makowska, M., Dziosa, K., 2024. Influence of different pyrolysis temperatures on chemical composition and graphite-like structure of biochar produced from biomass of green microalgae *Chlorella sp*. Environmental Technology & Innovation 35, 103667.
H.M. Meena, S. Kukreti, P. Jassal, Synthesis of a novel chitosan-TiO2 nanocomposite as an efficient adsorbent for the removal of methylene blue cationic dye from wastewater, J. Mol. Struct. 1319 (2025) 139420.
T.R. Menezes, K.M. Santos, H. Mao, K. Santos, J.F. De Conto, J.A. Reimer, S.M. Dariva, C. C. Santana, Efficient separation of carbon dioxide and methane in high-pressure and wet gas mixtures using Zr-MOF-808, Separation and Purification Technology 354 (2025) 129033.
Meng, S., Meng, F., Chi, H., Chen, H., Pang, A., 2023. A robust observer based on the nonlinear descriptor systems application to estimate the state of charge of lithium-ion batteries. J. Franklin Inst. 360 (16), 11397–11413.
Meskel, A.G., Kwikima, M.M., Meshesha, B.T., Habtu, N.G., Naik, S.C.S., Vellanki, B.P., 2024. Malachite green and methylene blue dye removal using modified bagasse fly ash: adsorption optimization studies. Environmental Challenges 14, 100829.
Mohan, H., Mohandoss, S., Prakash, A., Balasubramaniyan, N., Loganathan, S., Assadi, A. A., Khacef, A., 2024. Cold plasma assisted synthesis of spinel-$CoFe_2O_4$ nanoparticle with narrow bandgap and high magnetic activity. Inorg. Chem. Commun., 112754
Moradnejati, S., Soleiman-Beigi, M., Lemraski, E.G., Baghelani, M., 2024. Synthesis and application of natural asphalt sulfonic acid (NA-SO_3H) as a novel and reusable carbonaceous super adsorbent for rapid decolorization of aqueous dye solutions. Colloids Surf. A Physicochem. Eng. Asp. 690, 133741.
Moussavi, G., Hosseini, H., Alahabadi, A., 2013. The investigation of diazinon pesticide removal from contaminated water by adsorption onto NH_4Cl-induced activated carbon. Chem. Eng. J. 214, 172–179.
Murthy, T.K., Gowrishankar, B., Krishna, R.H., Chandraprabha, M., Mathew, B.B., 2020. Magnetic modification of coffee husk hydrochar for adsorptive removal of methylene blue: isotherms, kinetics and thermodynamic studies. Environmental Chemistry and Ecotoxicology 2, 205–212.
Nguyen, N.T.H., Nguyen, T.T.T., Nguyen, D.T.C., Van Tran, T., 2024. A comprehensive review on the production of durian fruit waste-derived bioadsorbents for water treatment. Chemosphere, 142801.
Ouaddari, H., Abbou, B., Lebkiri, I., Habsaoui, A., Ouzzine, M., Allah, R.F., 2024. Removal of Methylene Blue by adsorption onto natural and purified clays: kinetic and thermodynamic study. Chemical Physics Impact 8, 100405.
Ouznadji, Z.B., Sahmoune, M.N., Mezenner, N.Y., 2016. Adsorptive removal of diazinon: kinetic and equilibrium study. Desalination Water Treat. 57 (4), 1880–1889.
Palsaniya, K., Kumari, N., Dolia, S., Alvi, P., Choudhary, B., 2024. Tailoring quantum dots through citric acid modulation of $CoFe_2O_4$ ferrite. Mater. Chem. Phys. 313, 128820.
Pan, Y., Li, L., Yang, B., Ji, G., Zhao, Z., Zhang, H., Wang, F., Xia, M., Tao, Y., 2024. Adaptive structural modification of Zr-based MOF-808 via solvent and ligand engineering for enhanced fluoride ion adsorption efficiency. Separation and Purification Technology 348, 127731.
Qin, N., Tian, C., Carter, L., Tao, D., Zhou, Y., Zhang, F., 2024. Economical magnetic activated carbon for methylene blue removal from water. Sustainability 4, 100057.
Rabeie, B., Mahmoodi, N.M., 2024. Green and environmentally friendly architecture of starch-based ternary magnetic biocomposite (Starch/MIL100/$CoFe_2O_4$): synthesis and photocatalytic degradation of tetracycline and dye. Int. J. Biol. Macromol. 274, 133318. https://doi.org/10.1016/j.ijbiomac.2024.133318.
Raha, S., Ahmaruzzaman, M., 2020. Enhanced performance of a novel superparamagnetic g-C_3N_4/NiO/ZnO/Fe_3O_4 nanohybrid photocatalyst for removal of esomeprazole: effects of reaction parameters, co-existing substances and water matrices. Chem. Eng. J. 395, 124969.
Ren, H., Xia, X., Sun, Y., Zhai, Y., Zhang, Z., Wu, J., Li, J., Liu, M., 2024. Electrolyte engineering for the mass exfoliation of graphene oxide across wide oxidation degrees. J. Mater. Chem. A 12 (35), 23416–23424.
Revathi, A., Palanisamy, P., Boopathiraja, R., Sudha, D., 2024. Heterostructure of Fe_2O_3 doped Alstonia Scholaris wood waste derived activated carbon based electrode for supercapacitor applications. Diam. Relat. Mater. 144, 110953.
Saeed, F., Reddy, K.A., Sridhar, S., 2024. Efficient removal of environmentally hazardous heavy metal ions from water by NH_2-MIL-101-Fe and MOF-808-EDTA based polyether sulfone adsorbents. Chem. Eng. J. 497, 154688.
Saghir, S., Pu, C., Fu, E., Wang, Y., Xiao, Z., 2022. Synthesis of high surface area porous biochar obtained from pistachio shells for the efficient adsorption of organic dyes from polluted water. Surface. Interfac. 34, 102357.
Sağlam, S., Türk, F.N., Arslanoğlu, H., 2023. Use and applications of metal-organic frameworks (MOF) in dye adsorption. J. Environ. Chem. Eng., 110568

Saikia, R., Goswami, R., Bordoloi, N., Senapati, K.K., Pant, K.K., Kumar, M., Kataki, R., 2017. Removal of arsenic and fluoride from aqueous solution by biomass based activated biochar: optimization through response surface methodology. J. Environ. Chem. Eng. 5 (6), 5528–5539.

P. Saini, N. Chakinala, P.K. Surolia, A.G. Chakinala, Ultrasound-assisted enhanced adsorption of textile dyes with metal organic frameworks, Separation and Purification Technology 354 (2025) 128730.

Salehzadeh, H., Wantala, K., Shahmoradi, B., Maleki, A., Suwannaruang, T., Shivaraju, H.P., Mohammadi, E., Ren, G., Jenkins, D.F., Choi, H.-J., 2024. Enhanced photocatalytic degradation of diazinon using Ni: ZnO/Fe3O4 nanocomposite under solar light. J. Taiwan Inst. Chem. Eng. 161, 105528.

Salih, S.J., Ali, L.I.A., Hamad, W.M., 2024. Novel synthesis and characterization of magnesium-doped $CoFe_2O_4$ nanoparticles –SiO_2 –3-aminopropylethoxysilane– gallic acid magnetic nanocomposite for effective removal of cationic dyes. Arab. J. Chem. 17 (3), 105647. https://doi.org/10.1016/j.arabjc.2024.105647.

Selvaraj, S., Patrick, D.S., Manikandan, V., Vangari, G.A., Mohan, M.K., Navaneethan, M., 2024. Synergistic effects of La-doping on ZnO nanostructured photocatalysts for enhanced MB dye degradation. Surface. Interfac., 104538

Shadmehr, J., Zeinali, S., Tohidi, M., 2019. Synthesis of a chromium terephthalate metal organic framework and use as nanoporous adsorbent for removal of diazinon organophosphorus insecticide from aqueous media. J. Dispersion Sci. Technol.

Shamsizadeh, Z., Ehrampoush, M.H., Firouzabadi, Z.D., Zad, T.J., Molavi, F., Ebrahimi, A.A., Kamranifar, M., 2020. Fe_3O_4@ SiO_2 magnetic nanocomposites as adsorbents for removal of diazinon from aqueous solution: isotherm and kinetic study. Pigment Resin Technol. 49 (6), 457–464.

Sharma, K., Chakroborty, S., Pal, K., Panda, A.R., Malviya, J., Nath, N., Yadav, T., Parmar, A.S., Parmar, L., Asthana, N., 2024. Controllable synthesis of high-yield magnetic nanomaterials assisted dye adsorbents from waste-water treatment and applications. J. Mol. Struct., 137550

Shen, T., Luo, J., Zhang, S., Luo, X., 2015. Hierarchically mesostructured MIL-101 metal–organic frameworks with different mineralizing agents for adsorptive removal of methyl orange and methylene blue from aqueous solution. J. Environ. Chem. Eng. 3 (2), 1372–1383. https://doi.org/10.1016/j.jece.2014.12.006.

Shukla, A.K., Alam, J., Mallik, S., Ruokolainen, J., Kesari, K.K., Alhoshan, M., 2024. Optimization and prediction of dye adsorption utilising cross-linked chitosan-activated charcoal: response Surface Methodology and machine learning. J. Mol. Liq. 411, 125745.

Singh, E., Kumar, A., Mishra, R., You, S., Singh, L., Kumar, S., Kumar, R., 2021. Pyrolysis of waste biomass and plastics for production of biochar and its use for removal of heavy metals from aqueous solution. Bioresour. Technol. 320, 124278.

Singh, D., Singh, D., Mishra, V., Kushwaha, J., Sengar, M., Sinha, S., Singh, S., Giri, B.S., 2024. Strategies for biological treatment of waste water: a critical review. J. Clean. Prod., 142266

Sohrabi, N., Mohammadi, R., Ghassemzadeh, H.R., Heris, S.S.S., 2021. Equilibrium, kinetic and thermodynamic study of diazinon adsorption from water by clay/GO/Fe_3O_4: modeling and optimization based on response surface methodology and artificial neural network. J. Mol. Liq. 328, 115384. https://doi.org/10.1016/j.molliq.2021.115384.

Su, S., Zhang, R., Rao, J., Yu, J., Jiang, X., Wang, S., Yang, X., 2022. Fabrication of lanthanum-modified MOF-808 for phosphate and arsenic (V) removal from wastewater. J. Environ. Chem. Eng. 10 (5), 108527.

Su, T., Shang, H., Su, X., Sun, Z., Li, Y., Li, L., Zhang, Z., Geng, R., Chen, S., 2024a. High-capacity adsorption of organic dyes using separable pullulan gel encapsulated with PDA-modified ZIF-8. Carbohydrate Polymers 345, 122562.

Su, H., Hou, J., Zhu, J., Zhang, Y., Van der Bruggen, B., 2024b. Room-temperature aqueous synthesis of MOF-808 (Zr) for selective adsorption of dye mixtures. Separation and Purification Technology 333, 125957.

Su, X., Wang, X., Ge, Z., Bao, Z., Lin, L., Chen, Y., Dai, W., Sun, Y., Yuan, H., Yang, W., 2024c. KOH-activated biochar and chitosan composites for efficient adsorption of industrial dye pollutants. Chem. Eng. J. 486, 150387.

Subramani, S., Thinakaran, N., 2017. Isotherm, kinetic and thermodynamic studies on the adsorption behaviour of textile dyes onto chitosan. Process Saf. Environ. Protect. 106, 1–10.

Suratman, A., Astuti, D.N., Kusumastuti, P.P., Sudiono, S., Wijaya, H.W., Wibowo, A.H., 2024. Comprehensive study of thermochemical conversion of biomass okara into biochar. J. Anal. Appl. Pyrol., 106594

Tahir, H., Anwer, M., Khan, S., Saad, M., 2024. Enhancement of adsorption and photocatalytic activity of MgO nanoparticles for the treatment of textile dye using ultrasound assisted process by Response Surface Methodology. Desalination Water Treat., 100429

Tilaki, R.D., Kalakesh, L.R., Bavandi, S., Babanejad, I., Charati, J.Y., Rodriguez-Couto, S., 2020. Surfactant modified kaolinite (MK-BZK) as an adsorbent for the removal of diazinon from aqueous solutions. Desalination Water Treat. 196, 137–145. https://doi.org/10.5004/dwt.2020.25922.

Usman, A.R., Abduljabbar, A., Vithanage, M., Ok, Y.S., Ahmad, M., Ahmad, M., Elfaki, J., Abdulazeem, S.S., Al-Wabel, M.I., 2015. Biochar production from date palm waste: Charring temperature induced changes in composition and surface chemistry. J. Anal. Appl. Pyrol. 115, 392–400.

Varela, C.F., Gaona, I.S., Angarita, A.B., Rivera, A.M., Vargas, C.P., 2024. Ultra-fast and highly-reversible dyes adsorption using a prepared in-situ Fe (PO3) 2/biochar composite from corn cob. Ind. Crop. Prod. 218, 118966.

Viante, M.F., Zanela, T.M.P., Stoski, A., Muniz, E.C., Almeida, C.A.P., 2018. Magnetic microspheres composite from poly(ethylene terephthalate) (PET) waste: synthesis and characterization. J. Clean. Prod. 198, 979–986. https://doi.org/10.1016/j.jclepro.2018.07.101.

Wang, Y., Yu, Y., Li, H., Shen, C., 2016. Comparison study of phosphorus adsorption on different waste solids: fly ash, red mud and ferric–alum water treatment residues. Journal of Environmental Sciences 50, 79–86.

Wang, B., Hu, X., Li, L., Wang, H., Huang, H., Wang, R., Zhou, D., Yuan, J., Chen, L., 2023. Application and functionalization of toxic waste sludge-derived biochar for efficient phosphate separation from aqueous media: toxicity diminution, robust adsorption, and inner mechanism. Chem. Eng. J. 468, 143745. https://doi.org/10.1016/j.cej.2023.143745.

Wang, Y., Wu, J., Zhang, W., Zhong, L., Zhang, D., Yan, S., Shi, J., 2024a. Efficient Removal of Dibutyl Phthalate from Aqueous Solutions: Recent Advances in Adsorption and Oxidation Approaches. Reaction Chemistry & Engineering.

Wang, T., Fu, J., Gao, X., Li, G., Liu, D., 2024b. Pore engineering of MOF-808 for effective adsorption of roxarsone. Separation and Purification Technology 348, 127724.

Wang, Y., Wang, K., Wang, X., Zhao, Q., Jiang, J., Jiang, M., 2024c. Effect of different production methods on physicochemical properties and adsorption capacities of biochar from sewage sludge and kitchen waste: mechanism and correlation analysis. J. Hazard Mater. 461, 132690.

Wang, C., Tian, J., Cui, Y., Li, N., Cui, X., Yan, B., Chen, G., 2024d. Synergy of CoN_3 and CuN_3O_2 sites in single atom-decorated biochar for peroxymonosulfate activation: Accelerating the production of $SO_4^{\bullet-}$ and $^{\bullet}OH$. Chem. Eng. J. 496, 154133.

Wang, L., Zhao, H., Li, S., Guo, B., Huang, X., Gao, P., Xu, S., Ji, P., 2024e. Simultaneous removal of Methylene blue and Cadmium from aqueous solution by a novel sulfonated material: characterization, mechanism and application. J. Environ. Chem. Eng. 12 (1), 111706.

Wang, C., Zhang, B., Sun, X., Zhang, Y., Li, W., Yang, T., Ma, Y., Sun, Z., Li, T., 2024f. Fabrication of core–shell Fe_3O_4@ polypyrrole@ sodium dodecyl benzene sulfonate composite for high-performance adsorption of methylene blue and malachite green in water. Separation and Purification Technology 329, 125140.

Wei, X., Li, H., Zhang, X., Luo, C., Wang, H., Liu, L., Yue, C., 2024. Adsorption performance and mechanism of waste paper-derived phosphorus-rich carbon for separation of uranium from radioactive wastewater. J. Environ. Chem. Eng. 12 (2), 112486.

Yadav, S., Asthana, A., Chakraborty, R., Jain, B., Singh, A.K., Carabineiro, S.A., Susan, M. A.B.H., 2020. Cationic dye removal using novel magnetic/activated charcoal/β-cyclodextrin/alginate polymer nanocomposite. Nanomaterials 10 (1), 170.

Yadav, S., Rana, P., Bandichhor, R., Srivastava, A., Sharma, R.K., 2024. Unexplored catalytic potency of a magnetic $CoFe_2O_4$/Ni-BDC MOF composite for the one-pot sustainable synthesis of 5-substituted 1-H tetrazoles. Chem. Eng. J. 496, 153995.

Yang, J.-M., 2017. A facile approach to fabricate an immobilized-phosphate zirconium-based metal-organic framework composite (UiO-66-P) and its activity in the adsorption and separation of organic dyes. J. Colloid Interface Sci. 505, 178–185. https://doi.org/10.1016/j.jcis.2017.05.040.

Yang, B., Wheeler, J.I., Sorensen, B., Steagall, R., Nielson, T., Yao, J., Mendez-Arroyo, J., Ess, D.H., 2021. Computational determination of coordination structure impact on adsorption and acidity of pristine and sulfated MOF-808. Materials Advances 2 (13), 4246–4254.

Yang, P., Lu, Y., Zhang, H., Li, R., Hu, X., Shahab, A., Elnaggar, A.Y., Alrefaei, A.F., AlmutairiI, M.H., Ali, E., 2024. Effective removal of methylene blue and crystal violet by low-cost biomass derived from eucalyptus: characterization, experiments, and mechanism investigation. Environmental Technology & Innovation 33, 103459.

Ye, J., Jensen, M.M., Goonesekera, E.M., Yu, R., Smets, B.F., Valverde-Pérez, B., Domingo-Félez, C., 2024. Denitrifying communities enriched with mixed nitrogen oxides preferentially reduce N_2O under conditions of electron competition in wastewater. Chem. Eng. J. 498, 155292.

Yeddou Mezenner, N., Lagha, H., Kais, H., Trari, M., 2017. Biosorption of diazinon by a pre-treated alimentary industrial waste: equilibrium and kinetic modeling. Appl. Water Sci. 7, 4067–4076.

Yeganeh-Faal, A., Kadkhodaei, M., 2022. A new combustion method for the synthesis of copper oxide nano sheet and Fe_3O_4/CuO magnetic nanocomposite and its application in removal of diazinon pesticide. Results in Engineering 16, 100599. https://doi.org/10.1016/j.rineng.2022.100599.

Yildiz, H., 2024. The production of a novel adsorbent from forest waste (*Platanus orientalis L.*) for dye adsorption: adsorption process optimization and experimental design. Mater. Sci. Eng., B 304, 117366.

Yu, F., Pan, J., Li, Y., Yang, Y., Zhang, Z., Nie, J., Ma, J., 2022. Batch and continuous fixed-bed column adsorption of tetracycline by biochar/MOFs derivative covered with κ-carrageenan/calcium alginate hydrogels. J. Environ. Chem. Eng. 10 (3), 107996.

Yu, X., Feng, B., Yao, M., Peng, J., Yang, S., 2024. Recent progress in Modular electrochemical synthesis of hydrogen and high-value-added chemicals based on Solid redox Mediator. Small, 2310573.

Zain, N.S., Mahmoud, M., Khan, M.I., Zafar, F., Manzoor, S., Akhtar, N., Khan, M.A., El Azab, I.H., El-Bahy, Z.M., 2024. Machine learning-assisted optimization and evaluation of methylene blue adsorption kinetics on citrus aurantifolia leaves: insights from isotherm and thermodynamic studies. J. Taiwan Inst. Chem. Eng. 164, 105696.

Zare, M.R., Mengelizadeh, N., Aghdavodian, G., Zare, F., Ansari, Z., Hashemi, F., Moradalizadeh, S., 2024. Adsorption of acid red 18 from aqueous solutions by GO-$COFe_2O_4$: adsorption kinetic and isotherms, adsorption mechanism and adsorbent regeneration. Desalination Water Treat. 317, 100219. https://doi.org/10.1016/j.dwt.2024.100219.

Zhang, M., 2024. Enhanced fluoride removal using montmorillonite clay modified with CoFe2O4 and metal-organic frameworks. Environ. Res., 119389

Zhang, X., Lin, X., He, Y., Chen, Y., Luo, X., Shang, R., 2019. Study on adsorption of tetracycline by Cu-immobilized alginate adsorbent from water environment. Int. J. Biol. Macromol. 124, 418–428.

Zhang, Y., Cao, L., Zhang, J., Wang, J., Tian, G., 2024a. Eco-friendly preparation of biochar nanomaterials from waste walnut shell and their adsorption application. Ind. Crop. Prod. 213, 118462. https://doi.org/10.1016/j.indcrop.2024.118462.

Zhang, M., Yang, H., Zhao, D., Zeng, Y., Ding, Y., Gu, Z., Zhang, L., 2024b. Bimetallic biochar-MOFs composites catalyzing peroxydisulfate in sulfadiazine removal. Colloids Surf. A Physicochem. Eng. Asp. 694, 134124.

Zhao, X., Liu, S., Tang, Z., Niu, H., Cai, Y., Meng, W., Wu, F., Giesy, J.P., 2015. Synthesis of magnetic metal-organic framework (MOF) for efficient removal of organic dyes from water. Sci. Rep. 5 (1), 11849.